



Reconstructing the Observed Ionizing Photon Production Efficiency at $z \sim 2$ Using Stellar Population Models

Themiya Nanayakkara¹ , Jarle Brinchmann² , Karl Glazebrook³ , Rychard Bouwens¹ , Lisa Kewley^{4,5} , Kim-Vy Tran^{5,6,7,8} , Michael Cowley^{9,10} , Deanne Fisher³ , Glenn G. Kacprzak³ , Ivo Labbe³ , and Caroline Straatman¹¹

¹Leiden Observatory, Leiden University, P.O. Box 9513, 2300 RA Leiden, The Netherlands; themiyananayakkara@gmail.com

²Instituto de Astrofísica e Ciências do Espaço, Universidade do Porto, CAUP, Rua das Estrelas, PT4150-762 Porto, Portugal

³Centre for Astrophysics and Supercomputing, Swinburne University of Technology, Hawthorn, Victoria 3122, Australia

⁴Research School of Astronomy and Astrophysics, The Australian National University, Cotter Road, Weston Creek, ACT 2611, Australia

⁵ARC Centre of Excellence for All Sky Astrophysics in 3 Dimensions (ASTRO 3D), Canberra, Australian Capital Territory 2611, Australia

⁶School of Physics, University of New South Wales, Sydney, NSW 2052, Australia

⁷Department of Physics and Astronomy, Texas A&M University, College Station, TX 77843-4242, USA

⁸George P. and Cynthia Woods Mitchell Institute for Fundamental Physics and Astronomy, Texas A&M University, College Station, TX 77843-4242, USA

⁹Centre for Astrophysics, University of Southern Queensland, West Street, Toowoomba, QLD 4350, Australia

¹⁰School of Chemistry, Physics and Mechanical Engineering, Queensland University of Technology, Brisbane, QLD 4001, Australia

¹¹Sterrenkundig Observatorium, Universiteit Gent, Krijgslaan 281 S9, B-9000 Gent, Belgium

Received 2019 September 16; revised 2019 December 16; accepted 2019 December 25; published 2020 February 5

Abstract

The ionizing photon production efficiency, ξ_{ion} , is a critical parameter that provides a number of physical constraints to the nature of the early universe, including the contribution of galaxies to the timely completion of the reionization of the universe. Here, we use KECK/MOSFIRE and ZFOURGE multiband photometric data to explore the ξ_{ion} of a population of galaxies at $z \sim 2$ with $\log_{10}(M_*/M_{\odot}) \sim 9.0\text{--}11.5$. Our 130 H α detections show a median $\log_{10}(\xi_{\text{ion}} [\text{Hz erg}^{-1}])$ of 24.8 ± 0.5 when dust corrected using a Calzetti et al. dust prescription. Our values are typical of mass/magnitude selected ξ_{ion} values observed in the $z \sim 2$ universe. Using BPASSv2.2.1 and Starburst99 stellar population models with simple parametric star formation histories (SFH), we find that even with models that account for effects of stellar evolution with binaries/stellar rotation, model galaxies at $\log_{10}(\xi_{\text{ion}} [\text{Hz erg}^{-1}]) \lesssim 25.0$ have low H α equivalent widths (EWs) and redder colors compared to our $z \sim 2$ observed sample. We find that introducing starbursts to the SFHs resolve the tension with the models; however, due to the rapid time evolution of ξ_{ion} , H α EWs, and rest-frame optical colors, our Monte Carlo simulations of starbursts show that random distributions of starbursts in evolutionary time of galaxies are unlikely to explain the observed distribution. Thus, either our observed sample is specially selected based on their past SFH, or stellar models require additional mechanisms to reproduce the observed high UV luminosity of galaxies for a given production rate of hydrogen ionizing photons.

Unified Astronomy Thesaurus concepts: Galaxy evolution (594); Emission line galaxies (459); Galaxies (573); High-redshift galaxies (734)

1. Introduction

Current observational constraints suggest that the reionization of the universe occurred between $z \sim 20\text{--}6$ through the escape of ionizing photons (Lyman-continuum leakage) from young stellar populations in galaxies (Bouwens et al. 2015b; Finkelstein et al. 2015; Robertson et al. 2015). However, the exact source of these photons that are predominantly responsible for reionization is still under debate. To put constraints on mechanisms that drove the reionization, it is important to understand properties of the massive stars in this era and link how the production of ionizing photons from these stars influenced the ionization of surrounding regions leading to cosmic reionization (e.g., Barkana & Loeb 2006; Shin et al. 2008).

The ionizing photon production efficiency, ξ_{ion} , is defined as the production rate of Lyman-continuum photons ($\lambda_{\text{photon}} < 912 \text{ \AA}$) per unit Ultra-Violet (UV) continuum luminosity measured at 1500 \AA . ξ_{ion} provides a measure of hydrogen ionizing to nonionizing photon production rates and therefore is a measure of the ratio of massive to less-massive stars in stellar populations. ξ_{ion} combined with the UV luminosity density and the escape fraction of ionizing photons is required to compute the ionizing emissivity from galaxies to determine if and how galaxies drove

the reionization of the universe (e.g., Kuhlen & Faucher-Giguère 2012; Naidu et al. 2019). Additionally, ξ_{ion} is an ideal measurable to compare with stellar population model predictions, especially at the peak of the cosmic star formation rate density ($z \gtrsim 2$).

A direct measure of ξ_{ion} requires a flux measurement to be obtained below the Lyman limit. Even at $z \sim 2$, this requires extremely deep observations, suffers from high systematic errors, and given the high IGM absorption from observed sight-lines, can only be done on stacked samples (for a thorough analysis see Steidel et al. 2018, also see Reddy et al. 2016). Additionally, stellar population synthesis models can be used to calibrate the rest-UV continuum slope, β , with ξ_{ion} , and multiple studies have used the observed β to infer ξ_{ion} of high- z galaxies (Robertson et al. 2013; Bouwens et al. 2015a). However, β is also sensitive to dust, metallicity, and star formation histories (SFHs, e.g., Reddy et al. 2018) of galaxies, and thus, inferred ξ_{ion} values are influenced by related uncertainties. ξ_{ion} measurements from UV metal lines (Stark et al. 2017) requires deep exposures and suffer from further stellar population and photoionization uncertainties.

In ionization-bounded H II regions, under dust-free Case B recombination, H α emission is directly proportional to the number of Lyman-continuum photons produced by hot young

stars and has been used to estimate ξ_{ion} (e.g., Bouwens et al. 2016b; Matthee et al. 2017a; Nakajima et al. 2018; Shivaei et al. 2018). Studies that use narrowband imaging suffer from strong line contamination due to the close proximity of [N II] (and [S II]) $\lambda\lambda 6717\lambda 6731$ in the case of broadband imaging), which is usually corrected for using either empirical or model calibrations (Bouwens et al. 2016b; Matthee et al. 2017a). However, such calibrations are not well tested at $z \gtrsim 2$ and due to harder ionizing fields and variations in element abundances, emission-line ratios have shown to evolve from local calibrations (e.g., Steidel et al. 2014; Kewley et al. 2016; Strom et al. 2017). This could introduce systematic biases to line flux estimates. Additionally, accurate dust corrections to UV and nebular $H\alpha$ flux require a combination of multiwavelength photometry and Balmer-line ratios (see Shivaei et al. 2018); thus, spectroscopic measurements are crucial to obtain accurate estimates of the number of ionizing photons.

In this analysis, we take advantage of the recombination nature of the nebular $H\alpha$ emission line to estimate the amount of ionizing photons produced within galaxies. We combine MOSFIRE (McLean et al. 2012) spectroscopic observations by the ZFIRE survey (Tran et al. 2015; Nanayakkara et al. 2016) with multiwavelength photometry by the ZFOURGE survey (Straatman et al. 2016) to compute the ionizing photon production efficiency of a population of galaxies at $z \sim 2$. The paper is structured as follows: In Section 2, we present our sample. In Section 3, we present an analysis of the ξ_{ion} measurements with observed/derived properties of our sample. In Section 4, we briefly discuss our results, and we present our conclusions in Section 5. Unless otherwise stated, we assume a Chabrier (2003) IMF and a cosmology with $H_0 = 70 \text{ km s}^{-1} \text{ Mpc}^{-1}$, $\Omega_\Lambda = 0.7$ and $\Omega_m = 0.3$. All magnitudes are expressed using the AB system (Oke & Gunn 1983).

2. Sample Selection and Results

2.1. Survey Description

The spectroscopic data used in this analysis was obtained as a part of the ZFIRE survey (PIs K. Glazebrook, L. Kewley, K. Tran), which utilized the MOSFIRE instrument on Keck I telescope to obtain rest-frame optical spectra of mass/magnitude selected samples of galaxies around galaxy-rich environments at $z = 1.5\text{--}2.5$ (Yuan et al. 2014; Kacprzak et al. 2015; Tran et al. 2015; Alcorn et al. 2016). A thorough description of survey goals, sample selection, data reduction, flux calibration, and line flux measurements is presented in Nanayakkara et al. (2016). The ZFIRE sample in the COSMOS field (Scoville et al. 2007) comprises all 134 galaxies observed in MOSFIRE K band with secure $H\alpha$ detections ($\text{conf} = 3$, redshift determined by multiple emission lines) between $1.90 < z < 2.67$ with a 5σ line flux detection level $\sim 3 \times 10^{-18} \text{ erg s}^{-1} \text{ cm}^{-2} \text{ \AA}^{-1}$. The 80% stellar mass and Ks completeness of this sample are, respectively, $\log_{10}(M_*/M_\odot) > 9.3$ and $Ks < 24.11$. We remove four galaxies flagged as AGNs by Cowley et al. (2016). These AGN selections are based on infrared color-color classifications of Messias et al. (2012) and Rees et al. (2016) radio AGN activity index, and X-ray AGN selection criteria of (Szokoly et al. 2004), and we remove these galaxies from our sample. We consider the remaining 130 galaxies as our primary sample. Nanayakkara et al. (2016) showed that the $H\alpha$ selected sample contains no significant systematic biases toward SFH, stellar mass, and Ks band

magnitude based on the parent ZFOURGE sample (Straatman et al. 2016).

ZFIRE spectroscopic data supplements the ZFOURGE survey (PI I. Labbe), a Ks -selected deep 45-night photometric legacy survey carried out using the purpose built FourStar imager (Persson et al. 2013) in the 6.5 m *Magellan* Telescope. The survey covers 121 arcmin^2 in each of the COSMOS, UDS (Beckwith et al. 2006), and CDFS (Giacconi et al. 2001) legacy fields, reaching a 5σ depth of $Ks \leq 25.3 \text{ AB}$ and is complemented by the wealth of public multiwavelength photometric data (UV to far-infrared) available in these fields (Straatman et al. 2016).

2.2. ξ_{ion} Computation and Dust Corrections

For our analysis, we select all galaxies from the ZFIRE survey in the COSMOS field between $1.90 < z < 2.67$ with a $\text{conf} = 3$ and an $H\alpha$ signal-to-noise ratio (S/N) > 5 . We define ξ_{ion} as

$$\xi_{\text{ion}} = \frac{N(H)}{L_{\text{UV}}} [\text{Hz erg}^{-1}] \quad (1)$$

where $N(H)$ is the production rate of H ionizing photons per s , and L_{UV} is the intrinsic UV continuum luminosity at 1500 \AA .

In order to obtain the observed L_{UV} , we first refit ZFOURGE photometry using FAST++ (Schreiber et al. 2018a) at the spectroscopic redshifts and compute the UV luminosity at rest-frame 1500 \AA by fitting a power-law function to the best-fit spectral energy distribution (SED) model between $\Delta\lambda = 1400\text{--}1600 \text{ \AA}$. We use the exponential of the same power law as the UV continuum slope β .

Best-fit $A(V)$ values and stellar masses from FAST++ are computed using Bruzual & Charlot (2003) stellar population models with a Chabrier (2003) IMF, a truncated SFH with a constant and an exponentially declining SFH component, and a Calzetti et al. (2000) dust law. Galaxies are fixed at the spectroscopic redshift similar to Nanayakkara et al. (2016); however, we allow the stellar metallicity to vary as a free parameter between $Z = 0.004\text{--}0.02$, within which readily computed SFH models are available in FAST++. We use the FAST++ computed $A(V)$ values to obtain the intrinsic UV luminosity using the Calzetti et al. (2000) dust law. Additionally, in Table 1, we show that the choice of the SFH and the dust attenuation law in FAST++ may contribute up to $\sim 0.1 \pm 0.3$ and $\sim 0.02 \pm 0.1$ systematic offset to β and UV magnitude measurements, respectively.

$N(H)$ is computed following dust-free Case B recombination at an electron density of $n_e = 10^3 \text{ cm}^{-3}$ and temperature of $T = 10,000 \text{ K}$ assuming no escape of ionizing photons:

$$N(H) = \frac{L(H\alpha)}{C_B} [\text{s}^{-1}] \quad (2)$$

where $C_B = 1.36 \times 10^{-12} \text{ erg} = (\alpha_{\text{eff}H\alpha}/\alpha_{\text{eff}CB}) \times h\nu_{H\alpha}$ with $\alpha_{\text{eff}H\alpha} = 1.17 \times 10^{-13} \text{ cm}^3 \text{ s}^{-1}$, $\alpha_{\text{eff}CB} = 2.59 \times 10^{-13} \text{ cm}^3 \text{ s}^{-1}$, and $h\nu_{H\alpha} = 3.03 \times 10^{-12} \text{ erg}$ (Draine 2011). The intrinsic $H\alpha$ luminosity ($L(H\alpha)$ [erg s^{-1}]) is computed using the dust-corrected observed $H\alpha$ flux from the ZFIRE spectra as described below.

Table 1
Role of the Assumed SFH and Dust Law in FAST++

SFH 1	SFH 2	Dust Law 1	Dust Law 2	$\Delta\beta$	$\Delta M(\text{UV})$
Truncated	Exponentially declining	Calzetti et al. (2000)	Calzetti et al. (2000)	-0.003 ± 0.10	0.0007 ± 0.06
Truncated	Delayed τ	Calzetti et al. (2000)	Calzetti et al. (2000)	0.015 ± 0.11	0.007 ± 0.06
Truncated	Truncated	Calzetti et al. (2000)	Cardelli et al. (1989)	-0.05 ± 0.30	0.008 ± 0.10
Truncated	Truncated	Calzetti et al. (2000)	Kriek & Conroy (2013)	-0.07 ± 0.12	-0.02 ± 0.05

Note. Here, we show the median offset and σ_{NMAD} of β and $M(\text{UV})$ between different SFHs and dust laws computed using FAST++. Throughout the analysis best-fit SEDs derived assuming a truncated SFH with a Calzetti et al. (2000) dust law is used.

Table 2
 ξ_{ion} Sample Definitions

Set Name	N of Galaxies	UV Luminosity Dust-correction Law	H α Luminosity Dust-correction Law	Balmer Decrement from	Median $\log_{10}(\xi_{\text{ion}})$ [Hz erg $^{-1}$]
Set A	130	Calzetti et al. (2000)	Cardelli et al. (1989)	H α SFR stacks	24.83 ± 0.49
Set A	130	Calzetti et al. (2000)	Cardelli et al. (1989)	β stacks	24.77 ± 0.43
Set A	130	Calzetti et al. (2000)	Cardelli et al. (1989)	UV magnitude stacks	24.73 ± 0.49
Set A	130	Calzetti et al. (2000)	Cardelli et al. (1989)	Stellar mass stacks	24.79 ± 0.44
Set A	130	Calzetti et al. (2000)	Cardelli et al. (1989)	[O III] λ 5007/H α stacks	24.76 ± 0.45
Set A	130	Calzetti et al. (2000)	Cardelli et al. (1989)	UV+IR SFR stacks	24.68 ± 0.46
Set B	49	Calzetti et al. (2000)	Cardelli et al. (1989)	Individual observations	24.79 ± 0.58

Note. Here, we summarize the two samples used in our analysis.

2.2.1. Deriving Nebular Emission-line Corrections

We divide the sample into two sets and apply dust corrections following Cardelli et al. (1989) and Calzetti et al. (2000) dust laws for the nebular and stellar regions, respectively, as commonly done in the literature at $z \sim 2$ (e.g., Shivaie et al. 2018). We define our full sample as set A, which contains 130 galaxies with MOSFIRE H α detections observed in the K band. Only a subset of these galaxies were observed in MOSFIRE H band to obtain H β detections. We define the subsample of 49 galaxies from set A with H β detections ($S/N \geq 3$), as set B.

For our set B galaxies, we use the Cardelli et al. (1989) attenuation curve with the Balmer decrement values of the individual galaxies to obtain intrinsic H α luminosities following the Case B value of $f(\text{H}\alpha)/f(\text{H}\beta) = 2.86$.

We stack galaxies in set A with MOSFIRE H band observations in four H α SFRs bins and compute an average balmer decrement for each bin. Then, we compute the intrinsic H α luminosity for galaxies in each bin similar to set B using the average balmer decrement in each bin. Unless otherwise stated explicitly, we use this ξ_{ion} value for set A galaxies throughout the analysis. A summary of our galaxy sets is provided in Table 2.

2.3. The Observed Distribution of ξ_{ion}

In Figure 1, we show the distribution of ξ_{ion} in our sample. Galaxies in set A are shown with dust corrections applied with average balmer decrements from H α SFR stacks. The median of the distributions between set A and B is consistent within the scatter of the distribution (Table 2).

For comparison, in Figure 1, we also show the Shivaie et al. (2018) $z \sim 2$ galaxy sample, which has a median $\log_{10}(\xi_{\text{ion}})$ [Hz erg $^{-1}$] = 25.0 ± 0.4 with a stellar-mass completeness at $\log_{10}(M_*/M_\odot) \sim 9.5$. Our set A sample shows a similar distribution of ξ_{ion} to the Shivaie et al. (2018) sample albeit

with a slight bias toward low ξ_{ion} . Compared to Robertson et al. (2013) ξ_{ion} constraints to reionize the universe by $z \sim 6$, $\sim 80\%$ of our set A galaxies fall below this limit. Additionally, we show the distribution of ξ_{ion} for BPASSv2.2.1 (Eldridge et al. 2017) binary star constant SFH models at solar metallicity between 10 and 100 Myr from the onset of the star formation. This range shows the realistic distribution of ξ_{ion} from the onset of a star formation up to the point where the UV luminosity is stabilized in a constant SFH scenario. A majority of our galaxies in set A and set B have lower ξ_{ion} compared to these model predictions.

Our ξ_{ion} measurements are lower compared to model predictions, and such differences could be driven by differences in the stellar population/ISM properties (e.g., Kewley et al. 2019), calibration uncertainties, and/or the choice of the dust attenuation curve. In Nanayakkara et al. (2016), we showed that the relative calibration between ZFIRE spectra and ZFOURGE photometry agrees within $\lesssim 10\%$. We also visually inspected all spectra and the best-fit SEDs to determine if calibration offsets could drive the enhancement of ξ_{ion} and found in general good agreement between flux levels of the spectra and the SEDs. Therefore, we rule out calibration effects to have a dominant effect on the derived low ξ_{ion} of our sample. Even though we removed galaxies that showed evidence for AGN activity based on X-ray, infrared, and radio observations (Cowley et al. 2016), it is possible that our sample is contaminated by sub-dominant AGNs. If AGNs primarily contribute to an excess of UV flux, the low ξ_{ion} of our sample could be driven by effects of sub-dominant AGNs. However, AGN emission will also increase the H α emission, and thus, is unlikely to be a contributor to lowering ξ_{ion} of our sample.

In Figure 1, we show the median distribution of ξ_{ion} presented in this study along with other studies from the literature at $z \sim 2$ and higher. There are no statistically significant differences between our galaxies and Shivaie et al. (2018) ξ_{ion} analysis, and our analysis is independent of the type

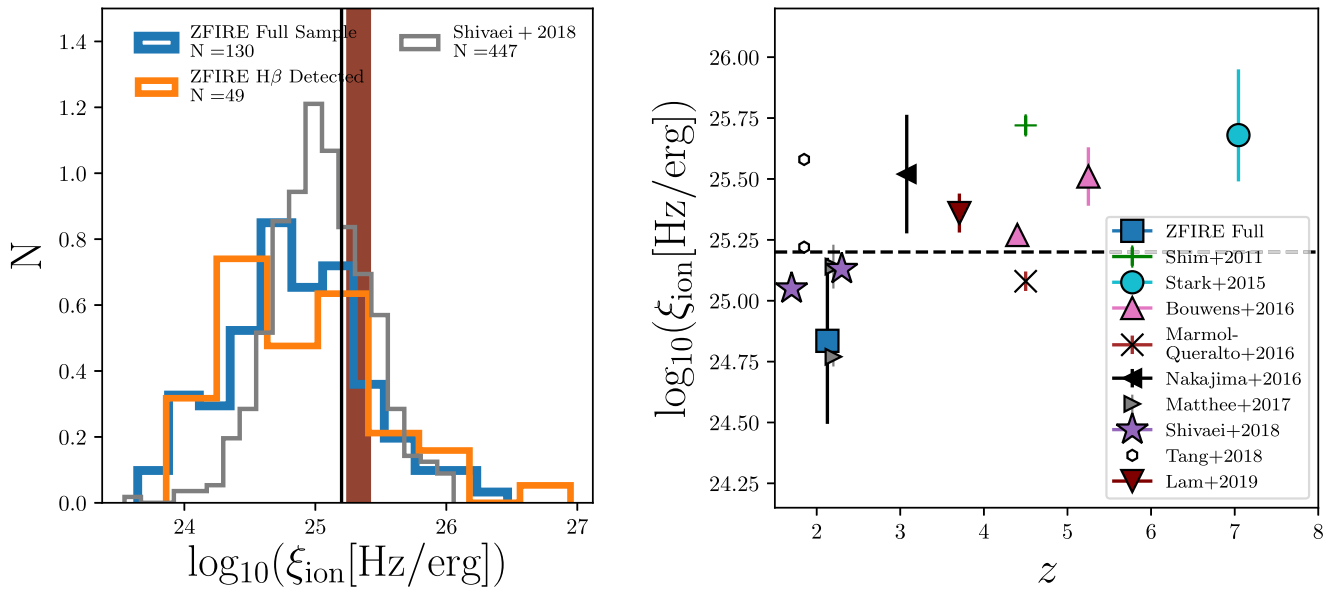


Figure 1. Left panel: the ξ_{ion} distribution of our sample. We show histograms of set A and set B galaxies along with the Shivaei et al. (2018) $z \sim 2$ sample. The maroon shading shows the ξ_{ion} distribution for a BPASSv2.2.1 binary stellar population model with a Salpeter (1955)-like IMF with an upper mass cut at $300 M_{\odot}$ at solar metallicity between 10 and 100 Myr of age. As a reference, we show the Robertson et al. (2013) $\log_{10}(\xi_{\text{ion}} [\text{Hz erg}^{-1}]) = 25.2$ (the ξ_{ion} needed to reionize the universe by $z \sim 6$) as a black vertical line. Right panel: the distribution of ξ_{ion} as a function of z for galaxies in our sample and a selected subset of galaxies from the literature: Shim et al. (2011), Stark et al. (2015), Bouwens et al. (2016b), Mármol-Queralto et al. (2016), Nakajima et al. (2016), Matthee et al. (2017a), Shivaei et al. (2018), Tang et al. (2019), and Lam et al. (2019) are shown for comparison. The dashed black horizontal line is the Robertson et al. (2013) $\log_{10}(\xi_{\text{ion}} [\text{Hz erg}^{-1}]) = 25.2$ value.

of stacks used to compute the average balmer decrement. Further, in Nanayakkara et al. (2016), we demonstrated that there were no statistically significant biases between the ZFOURGE COSMOS input sample and our $H\alpha$ detected sample (Set A) in terms of stellar mass or K_s magnitude. Tang et al. (2019) compute ξ_{ion} for a highly selective sample of galaxies between $z \sim 1.5$ – 3 , which are selected based on their extreme $[\text{O III}]\lambda 5007$ line properties and have stellar masses up to ~ 2 dex lower than our stellar-mass completeness. A majority of galaxies probed by Nakajima et al. (2016) are of high mass ($\log_{10}(M_{*}/M_{\odot}) > 9.0$); however, the sample is based on $\text{Ly}\alpha$ emitters with extreme $[\text{O III}]\lambda 5007$ emission. Therefore, it is not surprising that both Tang et al. (2019) and Nakajima et al. (2016) show on average higher ξ_{ion} compared to our sample.

Our ξ_{ion} are systematically lower than ξ_{ion} computed for $z \sim 4$ galaxies by Lam et al. (2019), $z \sim 5$ galaxies by Bouwens et al. (2016b), and $z \sim 7$ $\text{Ly}\alpha$ emitter by Stark et al. (2015). Thus, it is evident that our sample shows *typical* ξ_{ion} observed at $z \sim 2$ and is lower than what is observed in galaxies at $z \gtrsim 4$. This difference could be driven by a redshift evolution of ξ_{ion} (Matthee et al. 2017a), biases (i.e., mass incomplete samples) in sample selection of $z > 4$ observations, and/or differences in SFHs. We discuss this further in Section 4.4.

Next, we analyze the distribution of our sample with commonly probed correlations of ξ_{ion} in low- and high- z galaxies to investigate if such correlations also hold for our sample.

3. Analysis

3.1. Observed Correlations of ξ_{ion}

In Figure 2, we show the distribution of ξ_{ion} as a function of various galaxy properties. Along with individual galaxies, we

also bin in quartiles to show the median trend of ξ_{ion} with these galaxy properties. For each property, we stack galaxies with MOSFIRE H band observations in each of the quartiles to compute an average balmer decrement, which is used to correct for dust extinction of the nebular emission lines.

β . We observe a statistically significant moderate negative correlation between β and ξ_{ion} (Spearman rank-order correlation coefficient (Spearman 1904) of $r_s, p_s = -0.6, 1.3 \times 10^{-13}$ and $r_s, p_s = -0.5, 2.4 \times 10^{-4}$ for set A and B, respectively). Such a trend has also been observed at $z \sim 2$ (e.g., Shivaei et al. 2018) and at $z \sim 4$ (e.g., Bouwens et al. 2016b) but only for galaxies with $\beta < -2.0$, thus, for galaxies with relatively low dust attenuation compared to our sample. The lowest β observed for our sample is ~ -2.3 . We rule out line flux detection levels as a cause because we expect galaxies with low β to be highly star-forming dust-free young systems.

UV Magnitude. We compute the UV magnitude of our sample by integrating the fast++ best-fit sed template in the rest-frame using a box car filter at $1500 \pm 175 \text{ \AA}$. We do not find any evidence for any statistically significant correlations ($r_s, p_s = -0.1, 0.12$ and $r_s, p_s = 0.03, 0.83$ for set a and b, respectively) between UV magnitude and ξ_{ion} . The stacked galaxies in the UV magnitude bins also show a similar trend to the average trend of the individual galaxies. Eighty percent of our set a galaxies lie at UV magnitude > -18.8 ; thus, we cannot constrain the evolution of ξ_{ion} with UV magnitude for galaxies with fainter UV magnitudes, which is expected to dominate UV luminosity function at $z > 6$ (Bouwens et al. 2015b). Whether ξ_{ion} show a UV magnitude dependence is still unclear, with some studies showing evidence for no correlation at $z \sim 2$ – 5 (e.g Bouwens et al. 2016b; Shivaei et al. 2018; Lam et al. 2019) and some showing evidence for a correlation (Matthee et al. 2017b).

Stellar mass. Both set A and B galaxies show evidence for a statistically significant moderate negative correlation of

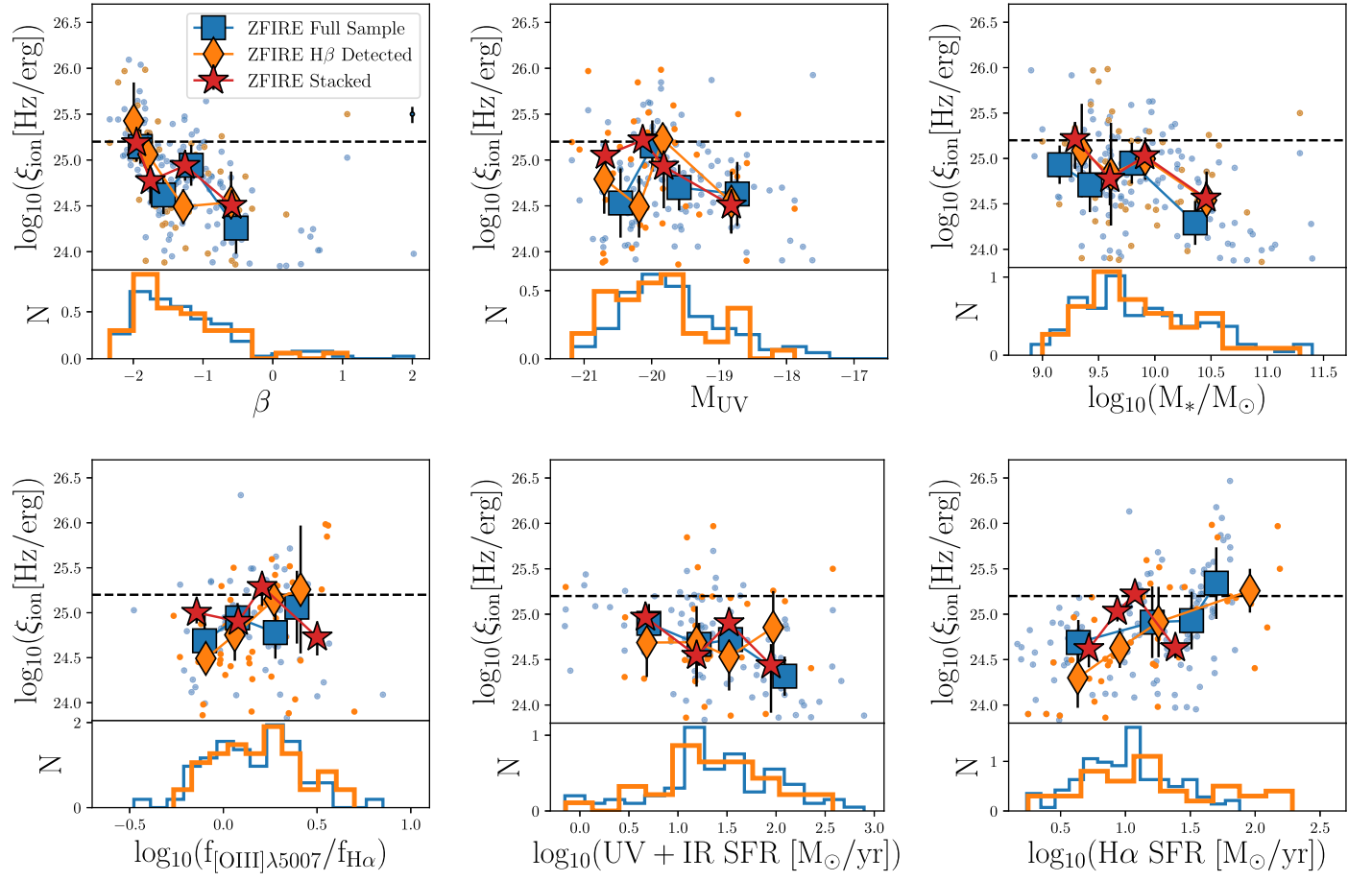


Figure 2. Distribution of ξ_{ion} of our sample as a function of various galaxy properties. Top left panel: UV continuum slope (β); top center panel: UV magnitude; top right panel: stellar mass; bottom left panel: $[\text{O III}]\lambda 5007/\text{H}\alpha$ ratio; bottom center panel: UV+IR SFR (only galaxies with at least one detection in photometric bands $>5 \mu\text{m}$ in the observed frame are shown); and bottom right panel: $\text{H}\alpha$ SFR. We bin galaxies in each of the considered properties and illustrate the median value in each bin and the 1σ scatter parameterized by the median absolute deviation. We additionally stack set A galaxies with MOSFIRE H band observations in four bins parameterized by the distribution in each of the galaxy properties and show the measurements computed for the stacks with associated errors computed using bootstrap resampling. A typical error bar for ξ_{ion} measurements of the individual galaxies is shown below the legend of the top left panel. The black horizontal dashed line shows Robertson et al. (2013) $\log_{10}(\xi_{\text{ion}} [\text{Hz erg}^{-1}]) = 25.2$ value. The lower panels of the figures illustrate the distribution of the values in each of the parameters.

ξ_{ion} with stellar mass ($r_s, p_s = -0.4, 2.1 \times 10^{-6}$ and $r_s, p_s = -0.3, 0.08$ for set A and B, respectively). A similar distribution is also evident for our stacked sample based on balmer decrements computed using stellar-mass stacks. As shown by the stellar-mass histograms, both set A and B galaxies show a similar distribution in stellar mass. We perform a two-sample K-S test between the parent ZFOURGE sample used for target selection of ZFIRE and set A and B galaxies and find that we cannot rule out the null hypothesis that both set A and set B galaxies are sampled from the same parent population. Therefore, we rule out any selection effects based on stellar-mass selection from ZFOURGE to play a role in driving these correlations.

In terms of the average trends, the lowest-mass galaxies show a slight enhancement in ξ_{ion} , but the distribution flattens out at higher stellar masses and shows a prominent decline at the highest stellar masses for both set A and B galaxies. The ZFIRE $\text{H}\alpha$ -detected sample reaches an 80% mass completeness at $\log(M_*/M_\odot) \sim 9.3$ (Nanayakkara et al. 2016), and set B also shows a similar completeness level. Therefore, we cannot make strong conclusions on the excess of ξ_{ion} in the lowest-mass bin, which has a median $\log(M_*/M_\odot) \sim 9.3 M_\odot$. Observations by Shivaie et al. (2018) and predictions by cosmological hydrodynamical simulations by Wilkins et al. (2016) show a

similar enhancement at lower stellar masses, but these can be attributed to a secondary effect compared to stellar population properties.

[O III] $\lambda 5007/\text{H}\alpha$ flux ratio. We select 58 galaxies with $S/N \geq 3$ for the $[\text{O III}]\lambda 5007$ emission line from our set A sample. At $z \sim 2$, $[\text{O III}]\lambda 5007$ and $\text{H}\beta$ both fall in the MOSFIRE H band, and all 49 galaxies in set B are also detected with $[\text{O III}]\lambda 5007$. We compute the intrinsic $[\text{O III}]\lambda 5007$ line flux similar to $\text{H}\alpha$, namely using the Cardelli et al. (1989) dust law with the balmer decrement computed for the stacked galaxies in each of the quartiles. Set A galaxies show no evidence for a statistically significant correlation ($r_s, p_s = 0.06, 0.6$), but set B galaxies do show a moderate positive correlation of ξ_{ion} with $[\text{O III}]\lambda 5007/\text{H}\alpha$ ratio ($r_s, p_s = 0.4, 2 \times 10^{-3}$). The stacked galaxies also show a flat distribution; however, the lowest $[\text{O III}]\lambda 5007/\text{H}\alpha$ bin shows a decline in ξ_{ion} .

$\text{H}\alpha$ luminosity traces the young ionizing stars in a galaxy while the conversion factor between the number of high-energy photons and the $[\text{O III}]\lambda 5007$ luminosity is strongly dependent on the metallicity and the ionizing parameter (e.g., Kewley et al. 2013). The observed correlation for set B suggests that galaxies with higher ionization parameters tend to have higher ξ_{ion} similar to observations by Shivaie et al. (2018); however,

we cannot make strong conclusions due to the absence of a correlation for set A galaxies.

SFR. Both $H\alpha$ emission-line luminosity and UV luminosity are direct traces of star formation with different age dependencies (e.g., Haydon et al. 2018); thus, we expect ξ_{ion} to show some correlation with the SFR. We select 98 galaxies from set A with detections in at least one of the *Spitzer*/*MIPS* or *Herschel*/*PACS* bands and use ZFOURGE UV+IR SFRs (Tomczak et al. 2016) to investigate dependencies of ξ_{ion} with SFR. All set B galaxies satisfy the above criteria. Our set A sample shows a moderate statistically significant negative correlation of ξ_{ion} with UV+IR SFR ($r_s, p_s = -0.5, 9.1 \times 10^{-7}$), while set B does not show any evidence for a statistically significant correlation ($r_s, p_s = 0.08, 0.65$).

In terms of $H\alpha$ SFRs, both set A and B galaxies show a statistically significant moderate positive correlation with ξ_{ion} ($r_s, p_s = 0.5, 6.9 \times 10^{-10}$ and $r_s, p_s = 0.6, 6.3 \times 10^{-7}$ for set A and B, respectively). The stacked galaxies show a similar positive trend; however, the highest SFR bin shows a decline in SFR, which is primarily driven by ~ 0.2 dex increase in UV luminosity in the highest SFR bin. Given both set A and B galaxies show similar distributions for UV+IR and $H\alpha$ SFRs, it is unlikely that a bias in SFR would drive the different observed correlations between UV+IR and $H\alpha$ SFRs.

Our analysis of ξ_{ion} with various galaxy observables/properties demonstrate that our sample does not show any strong trends with variables that are commonly used for selection (e.g., stellar mass, M_{UV}). The observed trends of ξ_{ion} are moderate at most and also agree well with other studies where available. We conclude that both the set A and B samples are relatively unbiased samples of star-forming galaxies at $z \sim 2$.

3.2. Combining ξ_{ion} with $H\alpha$ EW and Optical Colors

ξ_{ion} , $H\alpha$ equivalent width (EW), and rest-frame optical colors are diagnostics of specific SFR (sSFR) sensitive to different stellar masses. As shown by Equation (2), $N(H) \propto H\alpha$ and therefore is sensitive to young O-type stars with masses $\gtrsim 20 M_{\odot}$. The continuum at $H\alpha$ of a star-forming galaxy is dominated by red giant stars with masses $\sim 0.7\text{--}3 M_{\odot}$, while UV luminosity trace O and B type stars with masses $\gtrsim 3 M_{\odot}$. Therefore, $H\alpha$ EW traces the ratio of the short lived massive O stars to the older red giants stars, while ξ_{ion} traces the ratio of massive O-type stars to less-massive O and B type stars and are sensitive to the mass distribution in a stellar population at different parts of the IMF.

Given that the mass of the stars determine its main-sequence lifetime, $H\alpha$ EW and ξ_{ion} are both also sensitive to the age from the most recent starburst in a stellar population. The [340]–[550] color (box car filters at $3400 \pm 150 \text{ \AA}$ and $5500 \pm 150 \text{ \AA}$ chosen to avoid spectral regions with strong emission lines; see Appendix B in Nanayakkara et al. 2017, for further details) is sensitive to the ratio of bluer stars to redder stars. Thus, [340]–[550] color, $H\alpha$ EW, and ξ_{ion} are also sensitive to the SFH/age of a stellar population.

In this section, we combine the analysis of $H\alpha$ EW and [340]–[550] color with ξ_{ion} to investigate whether we can make stronger constraints on the nature of the stellar populations.

The $H\alpha$ EW and rest-frame optical colors of star-forming galaxies have been studied in detail as a tracer of high-mass stellar IMF and of stellar rotation and binaries in stellar populations (e.g., Kennicutt 1983; Hoversten & Glazebrook 2008; Gunawardhana et al. 2011; Nanayakkara et al. 2017).

From our full sample, we remove galaxies with multiple objects within the MOSFIRE slits or galaxies that had bright sources close to the slit edges and select 77 (out of which 31 are in Set B) galaxies to compute the $H\alpha$ EW using ZFOURGE *Ks* band photometry. We remove the $H\alpha$ flux contribution from the photometric flux and compute a continuum flux assuming that other emission lines within *Ks* band have a negligible contribution to the total photometry. We then approximate $H\alpha$ EW as the fraction between $H\alpha$ line flux and the continuum estimated from the photometry. In order to investigate any systematic offsets in computing $H\alpha$ EWs using ZFOURGE photometry, we select a subsample of 38 galaxies with confident *K* band continuum detections in MOSFIRE spectra (Nanayakkara et al. 2017) and compare the difference in $H\alpha$ EW. We find a good agreement between $H\alpha$ EWs computed using spectroscopically to photometrically determined continuum levels with a median $\Delta \log_{10}(\text{EW}) = -0.02 \pm 0.11 \text{ \AA}$. Additionally, we note that all ZFIRE spectra are corrected for slit loss using broadband photometry from *Hubble Space Telescope* (*HST*) F160W and FourStar *Ks* band fluxes (Nanayakkara et al. 2016).

3.2.1. Simple Parametric SFHs Using BPASS Stellar Population Models

We first use BPASSv2.2.1 binary stellar population models with simple parametric SFHs to compare with the distribution of our observed sample in ξ_{ion} , $H\alpha$ EW, and [340]–[550] color space. In Figure 3, we show the $H\alpha$ EW versus [340]–[550] color of our sample and expectations from BPASS stellar population models with Z_{\odot} and $1/20\text{th } Z_{\odot}$ metallicities. The models are computed for constant and exponentially increasing and decreasing SFHs with a Salpeter (1955) like IMF. Galaxies with high $H\alpha$ EW for a given [340]–[550] color prefer lower-metallicity tracks compared to galaxies with low $H\alpha$ EWs. The average distribution of galaxies in $H\alpha$ EW and [340]–[550] color can be explained by the BPASS models. However, we note that there is a fraction of galaxies with lower $H\alpha$ EWs and/or bluer optical colors than what is expected from the BPASS models. Including effects of random starbursts over smooth SFHs in stellar population models could explain this subset of galaxies (Nanayakkara et al. 2017), and we discuss this further in Section 3.2.2.

In Figure 3, we also show the distribution of $H\alpha$ EW and [340]–[550] color as a function of ξ_{ion} . In terms of $H\alpha$ EW, there is a statistically significant observed trend, where galaxies with higher $H\alpha$ EWs show higher ξ_{ion} values. This trend is expected because both axes trace the number of hydrogen ionizing photons in the nominator and therefore are correlated with each other. In order to verify that low S/N in the $H\alpha$ measurement does not lead to the observed correlation, we compute the Spearman’s rank correlation coefficient for galaxies with $H\alpha$ S/N > 10 and find that the statistically significant trend of $H\alpha$ EW with ξ_{ion} still holds.

In the center and right panels of Figure 3, we also show the same BPASS models that well described the observed distribution of $H\alpha$ EW and [340]–[550] color of our sample. The observed galaxies on average show higher $H\alpha$ EWs for a given ξ_{ion} , specially for galaxies with $\log_{10}(\xi_{\text{ion}}[\text{Hz erg}^{-1}]) < 25.0$. The models diverge from the data at $H\alpha$ EW $\lesssim 2.25 \text{ \AA}$ in $H\alpha$ EW versus ξ_{ion} space, while in $H\alpha$ EW and [340]–[550] color space, models only diverge from the data at $H\alpha$ EW $\lesssim 2.0 \text{ \AA}$.

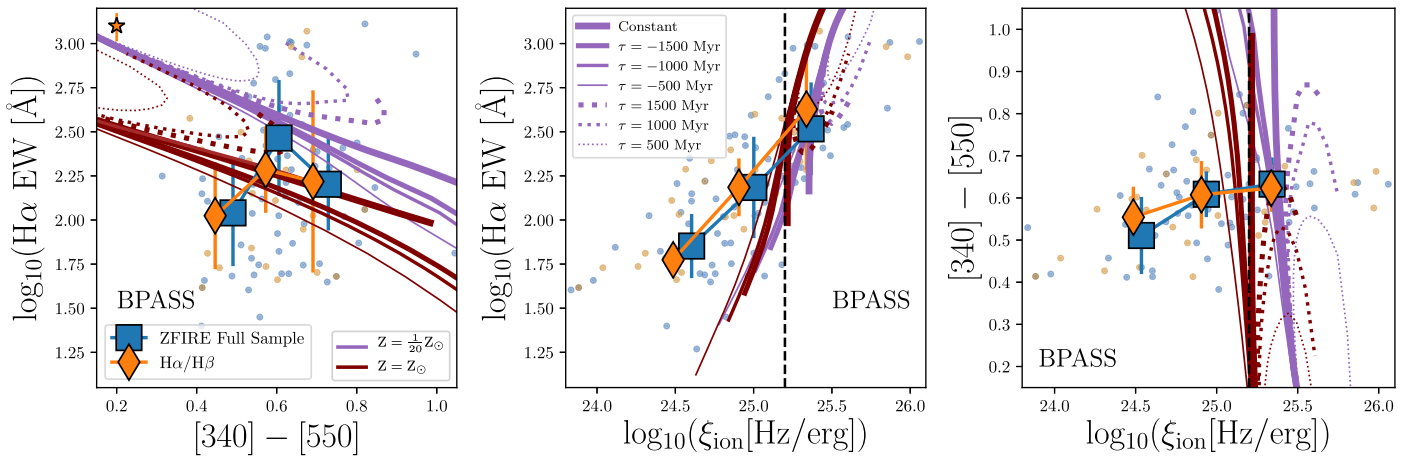


Figure 3. Left panel: $H\alpha$ EW as a function of dust-corrected $[340]-[550]$ color; center panel: $H\alpha$ EW; and right panel: dust-corrected rest-frame optical color ($[340]-[550]$) as a function of ξ_{ion} . Galaxies are binned in equal number bins in the x axis with the scatter parameterized by the median absolute deviation. We overlay stellar population models from BPASSv2.2.1 for constant SFH models ($1 M_{\odot} \text{ yr}^{-1}$) and exponentially increasing and decreasing SFHs with $\tau = 1500, 1000, 500$ Myr for Z_{\odot} and $1/20 Z_{\odot}$ metallicities. All models are computed for a Salpeter (1955) like $\Gamma = -1.35$ slope IMF for stellar masses in the range of $0.5-300 M_{\odot}$ and a $\Gamma = -0.3$ slope for masses in the range of $0.1-0.5 M_{\odot}$. All models terminate at $t \sim 3100$ Myr, which is the age of the universe at $z \sim 2$. The largest error bar for a single galaxy in the $H\beta$ -detected sample is shown by the top left star in the top left panel. The observed distribution of our galaxies in $H\alpha$ EW and rest-frame optical color space is well reproduced by the BPASS models by varying the SFH and the stellar metallicity; however, the predicted ξ_{ion} values are consistently too high for the observed $H\alpha$ EW and rest-frame optical colors.

ξ_{ion} versus $[340]-[550]$ color (Figure 3) shows evidence for a statistically significant moderate trend, where galaxies with higher ξ_{ion} show slightly redder optical colors. This suggests that in light weighted terms, optical colors of the high ξ_{ion} sample may be dominated by the older stellar populations. Therefore, if galaxies with high ξ_{ion} do harbor starbursts, the relative strength of the starburst compared to the past SFH should be low. Within the BPASS parametric SFHs explored in Figure 3, our observed galaxies with $\log_{10}(\xi_{\text{ion}}[\text{Hz erg}^{-1}]) < 25.0$ are bluer compared to the BPASS models.

BPASS model tracks show a strong dependence on Z in $H\alpha$ EW versus $[340]-[550]$ color space. At all times, the low- Z models have higher $H\alpha$ EWs compared to the Z_{\odot} models; however, low- Z models evolve fast in the $[340]-[550]$ colors and tend to be redder. The observed distribution of our galaxies are in general well explained by BPASS models the $H\alpha$ EW versus $[340]-[550]$ space by simply varying the Z and the exponential decay timescale of the SFH.

In $H\alpha$ EW versus ξ_{ion} and $[340]-[550]$ versus ξ_{ion} space, BPASS models do not well represent the observed data. The drop in $H\alpha$ EW for a given ξ_{ion} was too high in the BPASS models in order to match with the observed data. Additionally, model galaxies were too red at $\log_{10}(\xi_{\text{ion}}[\text{Hz erg}^{-1}]) \lesssim 25.0$. Since the observed distribution in $H\alpha$ EW versus $[340]-[550]$ space is matched well by the BPASS models, it seems likely that the balance between the production rate of hydrogen ionizing photons and the UV luminosity drives the discrepancy between the models and data. If BPASS models with parametric SFHs are to match with the observed distribution of galaxies, UV luminosity at fixed $H\alpha$ flux should decrease, thereby increasing the ξ_{ion} .

Can the discrepancy between the BPASS models and our observations be resolved by introducing more complex SFHs with starbursts? Given that our sample traces the typical star formation stellar-mass relation for $z \sim 2$ star-forming galaxies (Nanayakkara et al. 2016, 2017) of Tomczak et al. (2016), we expect simple parametric SFHs on average to be an accurate description of the SFHs of our systems. However, at $z \sim 2$, galaxies are at the peak of the star formation rate density, and

therefore, it is likely that a fraction of our galaxies may in fact be in a starburst phase. Next, we investigate the behavior of starbursts in ξ_{ion} , $H\alpha$ EW, and $[340]-[550]$ color space.

3.2.2. StarBursts Using Starburst99 Stellar Population Models

We use Starburst99 models with Geneva stellar tracks that incorporate effects of stellar rotation in stellar evolution (Leitherer et al. 2014) to analyze the effect of starbursts. We switch from BPASS to Starburst99 models for this analysis since we are able to perform finer time sampling at 1 Myr intervals in Starburst99, which is crucial to finely track the effect of starbursts.

In Figure 4, we investigate three different burst scenarios with varying burst strengths and burst lengths overlaid on constant SFH models. We tune the burst strengths and lengths to produce SFHs that cover the observed ξ_{ion} , $H\alpha$ EW, and $[340]-[550]$ color space, and our burst properties are in agreement with FIRE simulation predictions of starbursts (Sparre et al. 2017). A summary of these burst properties is provided in Table 3.

Short starbursts in the post-starburst phase are able to maintain the observed high $H\alpha$ EW of the galaxies while maintaining a $\log_{10}(\xi_{\text{ion}}[\text{Hz erg}^{-1}]) \gtrsim 24.8$. However, such bursts fail to reproduce the observed redder colors of the galaxies. Long-lived bursts produce post-starburst tracks that could explain a majority of galaxies with low ξ_{ion} that have relatively low $H\alpha$ EWs. Once multiple bursts are invoked in the last ~ 600 Myr of the SFH of the galaxies, galaxies in the post-starburst phase show a similar behavior to the individual burst case. By invoking starbursts with varying strengths and lengths, the observed distribution at $z \sim 2$ could be reproduced.

In Figures 5 and 6, we further investigate the effect of starbursts and the relative timescales on which our observed parameters change. At the onset of the starburst, driven by the increase in the H ionizing photon production rate, the $H\alpha$ EW and ξ_{ion} increase rapidly to their maximum values within ~ 3 Myr. UV luminosity takes ~ 10 Myr to stabilize during the starburst; thus, once a maximum ξ_{ion} is achieved at ~ 5 Myr,

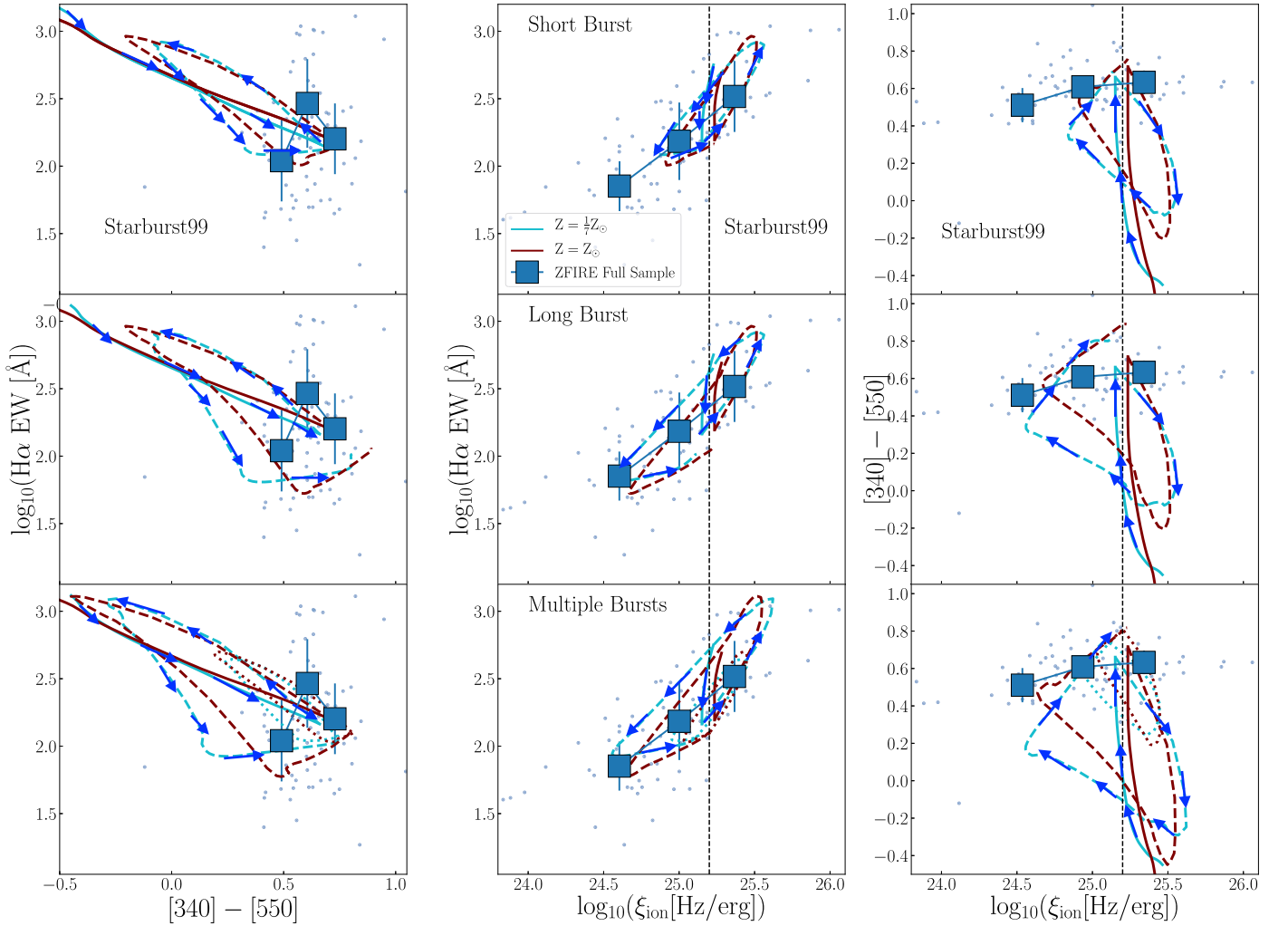


Figure 4. Behavior of starbursts. Left panel: $H\alpha$ EW vs. ξ_{ion} ; center panel: $[340]-[550]$ color vs. ξ_{ion} ; and right panel: $H\alpha$ EW vs. $[340]-[550]$ color space using the Starburst99 stellar evolution code with Geneva stellar tracks that account for effects of stellar rotation (Leitherer et al. 2014). Top panels: a single starburst of $\times 10$ the current SFR at $t = 2500$ Myr for $\Delta t = 10$ Myr; center panels: a single starburst of $\times 10$ the current SFR at $t = 2500$ Myr for $\Delta t = 100$ Myr; and bottom panels: two starbursts of $\times 20$ and $\times 5$ the current SFR at $t = 2500$ Myr and $t = 2800$ Myr for durations of $\Delta t = 20$ Myr and $\Delta t = 10$, respectively. Model tracks up to the point of the starburst are shown by the solid lines, and after the onset of the starburst, the tracks are shown by the dashed lines. If there is a secondary burst, the tracks after the onset of the secondary burst are shown by dotted lines. The arrows show how the model tracks evolve with time and are only shown for the $1/7 Z_{\odot}$ tracks. All models are normalized to the total mass formed by a $1 M_{\odot} \text{ yr}^{-1}$ constant SFH model at $z \sim 2$. Only set A galaxies are shown in the figure to improve clarity. The observed distribution of galaxies in this space can be explained well if most galaxies are in a longer duration starburst/post-starburst phase.

Table 3
Starburst99 Starburst Parameters Used in the Analysis

Name	Burst Time ^a (Myr)	Burst Strength	Burst Length (Myr)
Short	2500	$\times 10$	10
Long	2500	$\times 10$	100
Multiple	2500	$\times 20$	20
	2800	$\times 5$	10
Simulations ^b	200–3000	$\times 5-100$	10–100

Notes.

^a Defined from the onset of star formation.

^b 2–10 bursts are chosen randomly within these parameters to construct the SFH.

ξ_{ion} starts to drop gradually due to the increase in the UV luminosity. In the post-starburst phase, the drop in the H ionizing photon rate occurs very rapidly within the typical lifetime of massive O-type stars of ~ 10 Myr. Less-massive O

and B type stars that contribute to the UV luminosity are longer lived in the main sequence; thus, UV luminosity only reaches pre-burst levels ~ 100 Myr after the starburst. Therefore, after the end of the starburst, ξ_{ion} drops to a minimum and gradually rises up to the pre-burst levels driven by the reduction in UV luminosity.

The continuum at 6565 \AA is dominated by red giant stars, and therefore, from the onset of the starburst, the continuum flux gradually increases to a maximum until the end of the starburst. In the post-starburst phase, the continuum drops gradually and only reaches pre-burst continuum levels a few 100 Myr after the end of the starburst. Thus, $H\alpha$ EW show a similar time evolution to ξ_{ion} ; however, in the post-starburst phase, $H\alpha$ EW takes a longer time to reach pre-burst levels.

The $[340]-[550]$ color of the galaxies is also very sensitive to starbursts. Due to the massive blue stars formed by the starburst, galaxies show an almost instantaneous shift to blue colors at the onset of the starburst. Driven by the increase in post-main-sequence redder stars, the $[340]-[550]$ color gradually declines

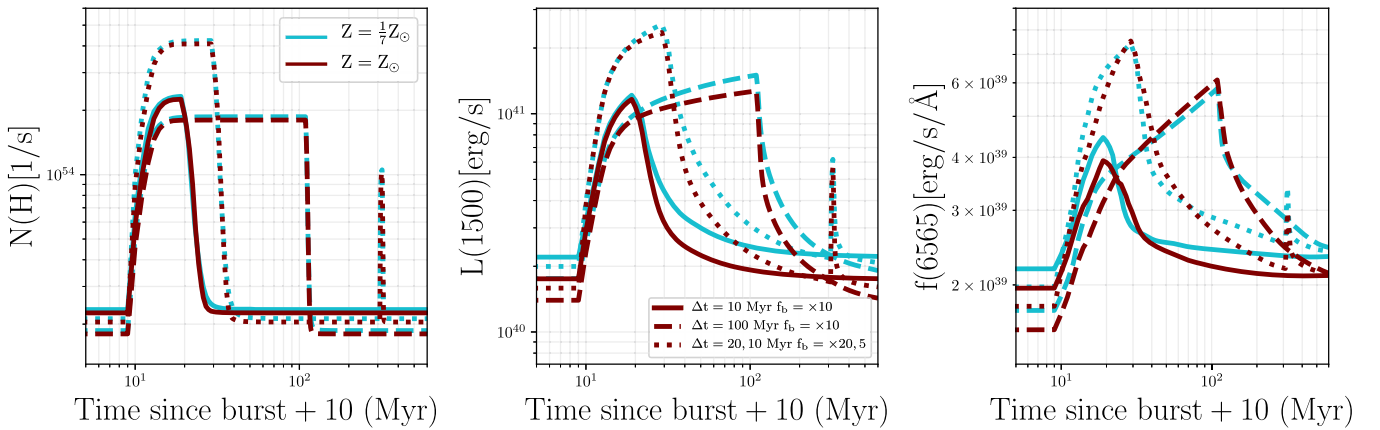


Figure 5. Time evolution. Left panel: the hydrogen ionizing photon production rate; center panel: the UV luminosity at 1500 Å; and right panel: the continuum flux at 6565 Å of Starburst99 models computed using Geneva stellar tracks that include effects of stellar rotation. Models are shown for three different burst scenarios with different burst strengths and lengths identical to Figure 4. In order to improve the clarity in time evolution, models are shown from $t-10$ Myr from the burst. Introducing bursts have a strong influence on all three variables; however, effects are spread over different timescales.

during the starburst until the end of the starburst. Galaxies turn redder within a very short timescale in the post-starburst phase, where stronger/longer-lived bursts show redder colors in the post-starburst phase compared to weaker/shorter-lived starbursts.

Within the context of Starburst99 models, we find metallicity to only have a weak influence on ξ_{ion} , H α EW, and [340]–[550] colors. The hydrogen ionizing photon production rate of the Geneva rotational models only increase by $\times \sim 1.04$ between Z_{\odot} to 1/7th Z_{\odot} models. The strongest influence of metallicity is on UV luminosity, where lower-metallicity stars show $\sim 25\%$ higher UV luminosity compared to higher-metallicity stars. This is possibly driven by stellar rotation, where higher-metallicity stars lose angular momentum faster due to their optically thick winds.

Starburst99 models with starbursts could reproduce our observed distribution of $z \sim 2$ galaxies in ξ_{ion} , H α EW, and [340]–[550] space. However, in order to satisfy the observables, a majority of our galaxies should lie in a post-starburst phase, and the time window on which the models populate the observed space is short compared to the total age of the universe at $z \sim 2$. We generate 1000 Starburst99 model galaxies with a constant SFH and overlay multiple bursts with randomly selected strengths and lengths at random times in its SFH and perform 10,000 bootstrap samples from the model grid between 1500 and 3100 Myr time window. A summary of the burst properties is also presented in Table 3.

In Figure 7, we show the 2D density distribution of our randomly sampled iterations. Random time sampling of constant+burst Starburst99 model galaxies is unable to reproduce the observed distribution of the $z \sim 2$ galaxies in ξ_{ion} , H α EW, and [340]–[550] space. In Figure 4, we showed that model tracks of starbursts do trace the observed distribution of galaxies in this space. However, given the very fast evolution of model tracks, not all values are equally likely. Thus, our random sampling exercise demonstrates that in a universe where galaxies undergo bursts at random times, it is unlikely to preferentially observe galaxies with high H α EWs, low ξ_{ion} , and blue optical colors.

We also note that our simulations are quite simplistic, and variations in Z , IMF, and other stellar model properties could lead to systematic limitations in our comparison of our simulations to the observed data. Implementing SED fitting of photometric data using nonparametric SFHs would allow us

to probe the variation in SFH of individual galaxies and investigate under exactly what conditions of stellar properties we could reproduce the observables (also see Chisholm et al. 2019). We leave this to future work.

4. Discussion

4.1. Observed Correlations of ξ_{ion}

In Section 3.1, we explored the variation of ξ_{ion} with various galaxy observables/properties. Our sample showed evidence for an enhancement of ξ_{ion} at $\beta < -1.5$, similar to previous observations (e.g., Bouwens et al. 2016b; Shivaie et al. 2018), and reaches the canonical $\log_{10}(\xi_{\text{ion}}[\text{Hz erg}^{-1}]) \sim 25.2$ value (Robertson et al. 2013) at $\beta \sim 2.0$. Thus, we expect an enhanced ξ_{ion} for galaxies with $\beta < -2.0$. Current observational constraints suggest $z > 6$ galaxies to have bluer UV slopes compared to their low- z counterparts (e.g., Bouwens et al. 2009), which may suggest an enhanced ξ_{ion} at $z > 6$.

β correlates with the UV/IR ratio and the UV reprocessed light in the far-IR, making it a suitable tracer for dust attenuation (Meurer et al. 1999). At $z > 2$, the infrared to UV flux ratio is shown to correlate with β and UV magnitude (Bouwens et al. 2016a), and therefore, it is possible for UV bright galaxies to have higher β values. Thus, we ask, is the enhancement of ξ_{ion} at lowest β values a result of enhancement of ξ_{ion} at faint UV magnitudes?

The relationship between ξ_{ion} and UV magnitude is important to constrain the processes that dominated the ionizing photon budget in the $z > 6$ universe. Faint UV galaxies are generally expected to have driven the reionization of the universe due to their high number density and high Lyman-continuum leakage (e.g., Duncan & Conselice 2015); however, recent empirically motivated models suggest that massive UV bright galaxies contributed to the bulk of the reionization budget (Naidu et al. 2019).

Once reionization is collectively constrained using ξ_{ion} , UV luminosity density, and the Lyman-continuum escape fraction, an evolution of ξ_{ion} with UV magnitude is currently not favored. This has been verified by some studies that show that ξ_{ion} has no correlation with UV magnitude (e.g., Bouwens et al. 2016b; Shivaie et al. 2018; Lam et al. 2019); thus, it seems unlikely that faint UV sources provide an additional contribution to reionization through elevated production of ionizing

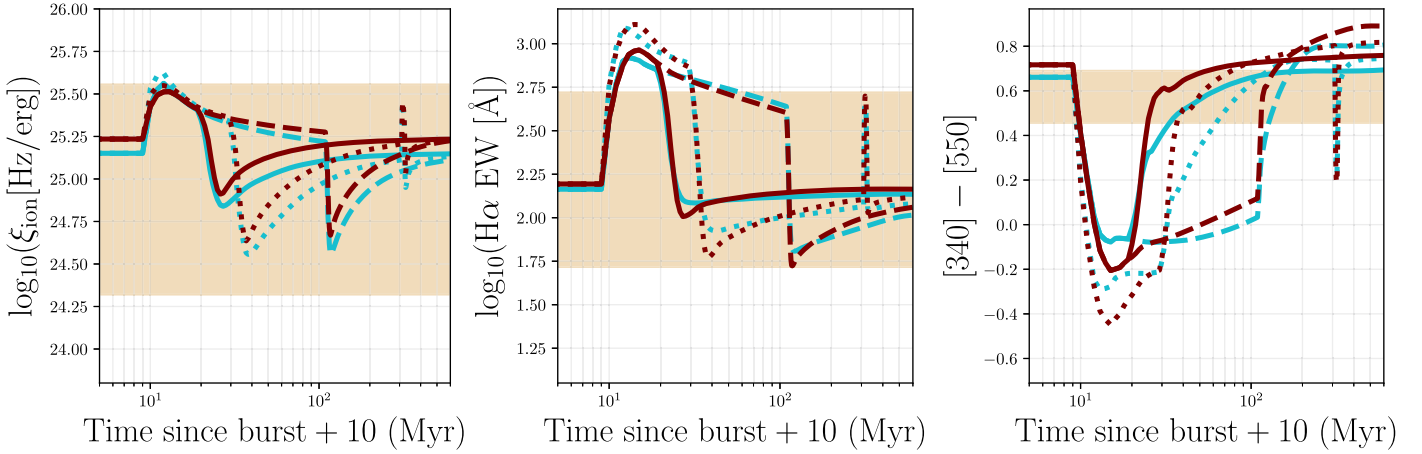


Figure 6. Time evolution. Left panel: ξ_{ion} ; center panel: H α EW; and right panel: [340]–[550] colors of Starburst99 models shown by Figure 5. For each variable, the observed median $\pm 1\sigma$ distribution of the $z \sim 2$ set A sample is shaded in yellow. The observed distribution of the galaxies can be reproduced by starbursts.

photons compared to UV bright sources. Our 80% completeness in UV magnitude at -18.8 is brighter than observed $z \sim 6$ median UV magnitude of $M_{\text{UV}} \sim -17.5$ (Bouwens et al. 2017); therefore, galaxies fainter than our detection level is capable of measuring are required to link with UV magnitude versus ξ_{ion} trends of galaxies observed in the reionization epoch.

An enhancement of ξ_{ion} at low stellar masses will also have implications to reionization processes in the $z > 6$ universe. At $z \sim 2$, our lowest stellar-mass bin shows an enhancement of ξ_{ion} ; however, it is also at the $\sim 80\%$ mass completeness level of our survey. Therefore, similar to other $z \sim 2$ studies (Matthee et al. 2017b; Shivaei et al. 2018), we cannot provide any constraints on whether there is an enhancement of ξ_{ion} at $\log_{10}(M_*/M_{\odot}) \lesssim 9.0$.

Accurate mass estimates require rest-frame optical coverage with $\lambda \gtrsim 5000 \text{ \AA}$ (Conroy 2013); thus, $z > 4$ stellar-mass estimates derived purely from *HST* photometry may lead to biases. Therefore, deep *Spitzer* or future *James Webb Space Telescope* observations of low-mass star-forming galaxies at $z > 4$ are crucial to determine, whether if there is a systematic increase in ξ_{ion} at lower masses leading up to the reionization era of the universe.

Our set B galaxies showed evidence for a moderate positive correlation of ξ_{ion} with [O III] $\lambda 5007$ /H α ratio. This correlation is driven by the presence of a strong correlation between [O III] $\lambda 5007$ and H α fluxes with $r_s, p_s = 0.9, 2.6 \times 10^{-20}$ (which is weaker for set A galaxies; $r_s, p_s = 0.7, 6.7 \times 10^{-9}$) and the absence of a statistically significant correlation between [O III] $\lambda 5007$ flux and UV luminosity ($r_s, p_s = -0.3, 0.06$). Set A galaxies show a moderate statistically significant negative correlation between [O III] $\lambda 5007$ flux and UV luminosity ($r_s, p_s = -0.4, 5 \times 10^{-4}$).

Shivaei et al. (2018) demonstrated an enhancement of ξ_{ion} for galaxies with high [O III]/[O II] ratios, high [O III]/H β ratios, and low [N II]/H α ratios. Similarly, Tang et al. (2019) showed ξ_{ion} to positively correlate with [O III] $\lambda 5007$ EW, and for [O III] $\lambda 5007$ EW to positively correlate with [O III]/[O II]. This translates to galaxies with a high ionization parameter and/or low stellar metallicity having high ξ_{ion} . If galaxies have higher hydrogen ionizing photon densities compared to their hydrogen densities, at fixed SFR and ISM conditions, naturally the ionizing photon production rate would be higher.

Therefore, such an enhancement of ξ_{ion} at a higher ionization parameter is expected and is possibly driven by the harder ionizing spectrum generated by the low-metallicity stars due to less metal blanketing in stellar atmospheres and conservation of angular momentum due to weaker optically thick stellar winds leading to longer main-sequence lifetimes (e.g., Eldridge et al. 2017).

Our analysis did not show strong evidence for ξ_{ion} to vary as a function of UV+IR SFR. Since both SFR and ξ_{ion} are sensitive to the production rate of ionizing photons, a correlation between H α SFR and ξ_{ion} is expected. However, ξ_{ion} is also sensitive to the stellar mass of young stars which contribute to the UV luminosity and, thus, is a proxy for the sSFR. In the stellar-mass star formation relation (Tomczak et al. 2016), high-mass galaxies show high SFRs; therefore, it is reasonable to expect ξ_{ion} to also show a flat distribution with the SFR. In terms of the time evolution of ξ_{ion} , stellar population models with parametric SFHs follow a smooth evolution, and, in a constant SFH scenario, ξ_{ion} will stabilize once the UV luminosity stabilizes. If galaxies undergo sudden bursts in their SFHs, the increase in SFR will be followed by an immediate increase in ξ_{ion} for a short period of time, after which ξ_{ion} will reduce and stabilize independent of the SFR.

4.2. Completeness of Our Observed Sample

In this analysis, we presented 130 H α emitters selected for spectroscopy from the ZFOURGE survey with a 80% stellar-mass completeness at $\log(M_*/M_{\odot}) \sim 9.3$. Our MOSFIRE spectroscopy sampled the $z \sim 2$ large scale structure in the COSMOS field (Spitler et al. 2012; Yuan et al. 2014) and our H α spectroscopic detection rate is similar to within 1% (Nanayakkara et al. 2016) of the rate expected by the photometric redshift probability distribution functions computed using EAZY (Brammer et al. 2008). Additionally, we found that the H α S/N of our sample peak at ~ 20 and that $\sim 81\%$ of our sample show a S/N of > 10 reaching a 3σ H α SFR detection limit at $\sim 4 M_{\odot} \text{ yr}^{-1}$. Thus, we conclude that our sample has a high spectroscopic completeness based on our stellar mass/ K_s magnitude based photometric pre-selection.

In Figure 8, we show the EAZY derived rest-frame $U - V$ versus $V - J$ colors of our spectroscopic sample with H α EW measurements. Compared to the ZFOURGE COSMOS sample at $1.90 < z_{\text{EAZY}} < 2.66$ (the redshift window where H α falls in

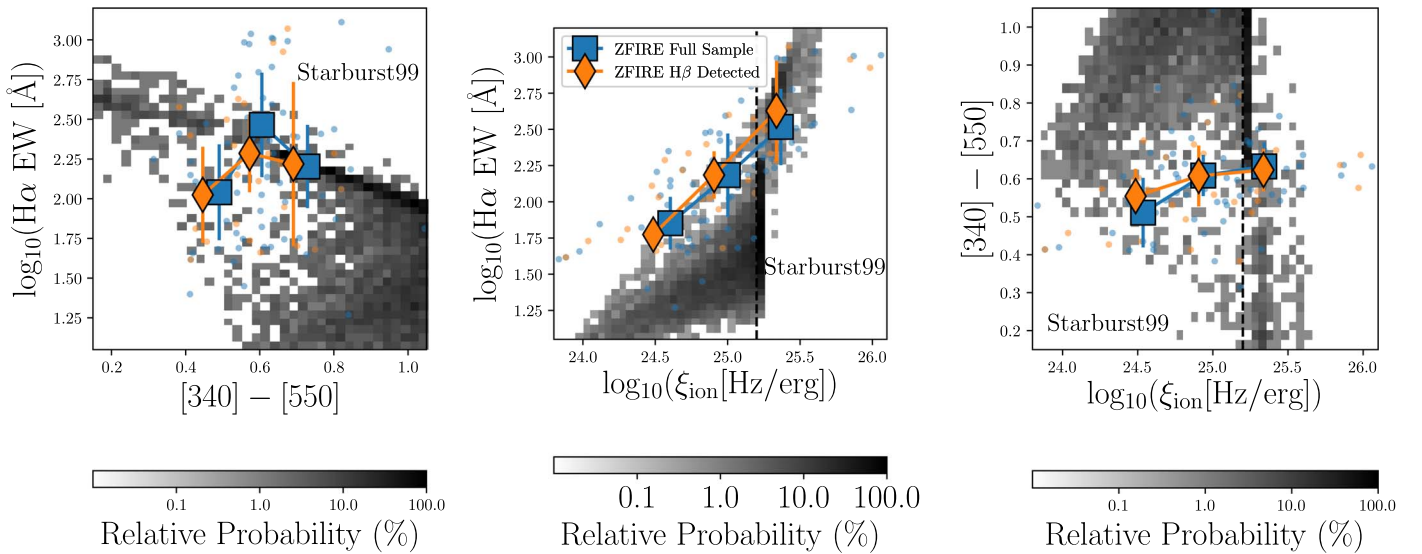


Figure 7. Probability distribution of 10,000 random realizations of 1000 Starburst99 model galaxies with constant+burst SFHs. Left panel: $H\alpha$ EW vs. $[340]-[550]$ color; center panel: $H\alpha$ EW vs. ξ_{ion} ; and right panel: $[340]-[550]$ color vs. ξ_{ion} space. Models are computed using Geneva stellar tracks at $\sim 0.6 M_{\odot}$ that account for effects of stellar rotation with a Salpeter (1955)-like high-mass IMF. Multiple bursts (randomly chosen between 2 and 10) with randomly chosen strengths ($\times 5-100$) and lengths ($\Delta t = 10-100$ Myr) are overlaid on the constant SFH models at random times between $t = 200-3000$ Myr. All models are normalized to the total mass formed by a $1 M_{\odot} \text{ yr}^{-1}$ constant SFH model at $z \sim 2$ and are sampled in 1 Myr time steps. The final grid contains $\sim 1.6 \times 10^6$ steps between 1500 and 3100 Myr, out of which 10,000 random iterations are selected with replacement. A 2D density distribution of the selected values is shown as a relative probability distribution by the gray-scale 2D histogram.

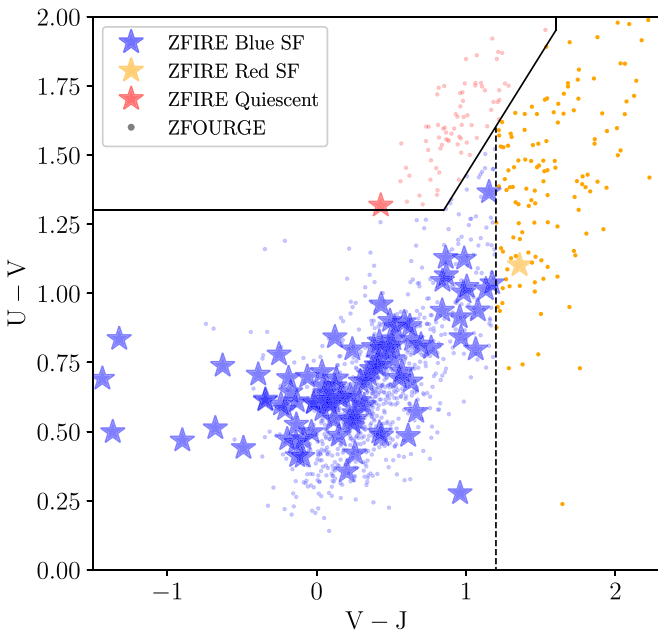


Figure 8. The rest-frame $U - V$ vs. $V - J$ color distribution of the 102 ZFIRE $z \sim 2$ galaxies used in the ξ_{ion} , $H\alpha$ EW, and $[340]-[550]$ color analysis. We also show the ZFOURGE parent population at $1.90 < z_{\text{EAZY}} < 2.66$ with $\log_{10}(M_{*}/M_{\odot}) > 9.3$ and $K_s < 24.78$. Galaxies are divided into blue star-forming (SF), red star-forming, and quiescent bins following Spitler et al. (2014) criteria. All rest-frame colors are derived using EAZY (Brammer et al. 2008). Our observed sample show a strong bias toward blue star-forming galaxies in this epoch.

MOSFIRE K band) with $\log_{10}(M_{*}/M_{\odot}) > 9.3$ and $K_s < 24.78$ (which are respectively the $\sim 80\%$ stellar-mass and K_s completeness of the spectroscopic sample), the majority of galaxies used in this analysis are blue star-forming systems. The $U - V$ versus $V - J$ color space can be used to distinguish between red (dusty) star-forming galaxies and passively evolving

galaxies (e.g., Labbé et al. 2007; Williams et al. 2009; Spitler et al. 2014). Our $H\alpha$ EW lacks red star-forming systems, which at high- z tend to be high-mass or high-SFR galaxies (Straatman et al. 2016). The bluest $V - J$ colors of our sample are dominated by the lowest-mass systems.

The lack of red star-forming galaxies in our $H\alpha$ EW sample may translate to a lack of galaxies with low sSFRs. Low sSFR galaxies would have low $H\alpha$ EWs, low ξ_{ion} , and redder $[340]-[550]$ colors. Therefore, including red star-forming galaxies in our sample may move the average trends toward regions populated by exponentially declining SFHs with low τ values. However, our parametric SFHs or burst SFH simulation results will still not agree with the individual nor average trends of blue star-forming galaxies. Within the context of blue star-forming galaxies at $z \sim 2$, we can rule out selection effects to have a strong influence on our observed correlations of ξ_{ion} with various galaxy properties explored in this analysis.

4.3. Dust Related Uncertainties in the ξ_{ion} Distribution

In Figure 1, we showed that $\sim 84\%$ of our sample fall below $\log_{10}(\xi_{\text{ion}} [\text{Hz erg}^{-1}]) = 25.2$, which is estimated as the ξ_{ion} required to reionize the universe by $z \sim 6$ under current observational constraints (Robertson et al. 2013). Our distribution of ξ_{ion} is also similar to the analysis by Shivaeei et al. (2018), which used MOSFIRE spectroscopic data from the MOSDEF survey (Kriek et al. 2015). In terms of spectroscopic completeness and accurate $H\alpha$ line flux estimates through high-quality spectroscopy and dust corrections, both our and Shivaeei et al. (2018)'s analyses provide strong constraints to the ξ_{ion} in the $z \sim 2$ universe for stellar-mass complete samples and also agrees well with narrowband emission-line-selected analysis by Matthee et al. (2017a).

The choice of the dust attenuation law plays a role on ξ_{ion} measurements. If the UV luminosity is corrected using an attenuation curve steeper than that of Calzetti et al. (2000), the dust-corrected UV luminosity will be lower, which will

increase the observed ξ_{ion} (e.g., Bouwens et al. 2016a). In terms of uncertainties related to the choice of dust attenuation curve, Shivaie et al. (2018) demonstrated that effects to ξ_{ion} are on the order of $\lesssim 0.2$ dex. Secondary dependence of dust attenuation on metallicity of galaxies (e.g., Reddy et al. 2018) may introduce additional complexities to the choice of the dust law, thus, with selective selection of dust attenuation law based on galaxy parameters may contribute to higher intrinsic ξ_{ion} .

Differential attenuation between nebular and stellar components also contributes to additional uncertainties in ξ_{ion} measurements. If the young stars reside near the stellar birth clouds, the nebular component in galaxies will undergo extra attenuation compared to the older stellar regions that contribute to the stellar continuum (e.g., Calzetti et al. 1994). Accurate determination of this absorption factor requires multiple Balmer emission-line ratios, and may also show a dependence on galaxy properties such as the SFR (Reddy et al. 2015).

4.4. z Evolution of ξ_{ion}

Our observed $z \sim 2$ ξ_{ion} measurements are ~ 0.5 dex smaller compared to $z > 4$ estimates. Matthee et al. (2017a) argues that one possibility for this observed discrepancy could be a redshift evolution of ξ_{ion} . Such an evolution may be justified if the SFHs of galaxies at $z > 4$ are either dominated by exponentially rising SFHs or if they are very chaotic with frequent starbursts. As we discussed in Section 3.2.2, starbursts would drive ξ_{ion} to increase rapidly within shorter timescales driven by an increase in the number of hydrogen ionizing photons. Thus, in this scenario, we would expect $z \sim 2$ star-forming galaxies to have exponentially declining SFHs dominated by relatively older stellar populations with high-UV luminosity, which would decrease ξ_{ion} .

In Section 3.2.2, we discussed in detail how starbursts affect the evolution of ξ_{ion} . Even with single or multiple starbursts with varying strengths, the time window in which ξ_{ion} would reach $\log_{10}(\xi_{\text{ion}} [\text{Hz erg}^{-1}]) > 25.5$ is very short and is within timescales of a few Myr. This is driven by the rapidly increasing contribution from the O and B type stars to the UV luminosity, which takes a longer time to stabilize compared to the more massive O stars that contribute to the hydrogen ionizing photons. Therefore, even if multiple starbursts do contribute to an increase of ξ_{ion} in $z > 4$ galaxies, the effects will be relatively short lived, and it is unlikely for starbursts to drive the high ξ_{ion} measurements.

4.4.1. Selection Effects in High- z ξ_{ion} Estimates

Driven by expectations from current stellar population models, we expect differences in selection functions of galaxies to play a dominant role in driving the differences in ξ_{ion} between $z \sim 2$ and $z > 4$. Observational estimates of ξ_{ion} at $z \sim 7$ are obtained through highly selective samples of extreme [O III] $\lambda 5007$ +H β emitters (Stark et al. 2015); thus, the observed high ξ_{ion} may not represent typical galaxy populations in the reionization era.

$z \gtrsim 4$ photometric samples selected based on color selection through strong H α + [N II] contamination on the *Spitzer*/IRAC bands (e.g., Shim et al. 2011; Bouwens et al. 2016b) would be biased toward strong H α emitters. Additionally, the IRAC bands used to estimate the H α flux are contaminated by [N II] and [S II] $\lambda 6717\lambda 6731$ emission lines. Hard ionizing radiation fields and high ISM pressures in young stellar systems may

lead to enhancements in [N II]/H α ratios (e.g., Kewley et al. 2016), which could lead to an overestimate of the H α flux if a fixed nonevolving [N II]/H α ratio is used for the correction.

The Lam et al. (2019) spectroscopic sample is based on the MUSE Deep (Inami et al. 2017) and MUSE Wide (Urrutia et al. 2019) surveys, where spectroscopic redshifts of galaxies at $z > 4$ are primarily determined through Ly α . The Nakajima et al. (2016) sample also consists of Ly α emitters and Lyman break galaxies and, thus, introduces a strong sample selection bias (e.g. Erb et al. 2016).

$z \sim 2$ galaxies based on extreme [O III] $\lambda 5007$ emitters show ξ_{ion} typical of $z > 4$ samples and strong positive correlations with [O III] $\lambda 5007$ EW (Tang et al. 2019). Therefore, it is likely that current high- z ξ_{ion} measurements are biased toward strong line emitters. Additionally, dust attenuation uncertainties further complicate ξ_{ion} estimates at these redshifts since such properties for most of these galaxies at $z > 3$ are not well constrained.

The observed correlation of ξ_{ion} with [O III] $\lambda 5007$, and H α EWs (see also Tang et al. 2019) suggest that current $z > 4$ ξ_{ion} measurements may be biased toward strong line emitters. If a majority of galaxies at higher redshifts do show strong ionizing properties, the observed high ξ_{ion} of $z > 4$ galaxies may be typical of the high- z universe. However, recent results have demonstrated that the observed diversity of galaxies in the $z \gtrsim 4$ universe is higher than what was previously expected (e.g., Spitler et al. 2014; Straatman et al. 2014; Glazebrook et al. 2017; Schreiber et al. 2018a, 2018b; Wang et al. 2019). Therefore, deeper spectroscopic explorations of the $z > 4$ universe are essential to build up representative samples of galaxies to accurately determine if there is an enhancement of ξ_{ion} with z .

4.4.2. Expectation from Current Stellar Population Models

In addition to selection effects biasing $z > 4$ observations, it is also important to consider if current stellar population models lack a sufficient amount of ionizing photons to reproduce high ξ_{ion} . Models may lack mechanisms/stellar types that may be prominent in galaxies in the early universe that contribute to an increase of hydrogen ionizing photons. $z \sim 0$ (e.g., Kewley et al. 2001; Senchyna et al. 2017) and $z \sim 2-4$ (e.g., Nanayakkara et al. 2019) studies have shown that stellar population models may lack mechanisms that produce high-energy photons in the EUV, which are required to produce observed emission-line ratios such as [S II] $\lambda 6717\lambda 6731$ /H α and observed He II $\lambda 1640$ spectral features (also see Section 5.3 of Kewley et al. 2019 for a detailed discussion on current limitations of stellar populations models). Including effects of X-ray binaries (e.g., Schaerer et al. 2019) and stripped stars (e.g., Götzberg et al. 2019) in stellar population synthesis models has been shown to increase the production of ionizing photons. Therefore, self consistent treatment of stellar evolution with rotation and binaries that contribute to such phenomena is crucial to make strong constraints on the nature of stellar populations in high- z galaxies.

Additionally, shallower slopes at the high-mass end of the stellar IMF in galaxies in the early universe will contribute to extra ionizing photons resulting in higher ξ_{ion} . However, currently, there are no observational constraints to the high-mass stellar IMF at higher redshifts, and investigating changes in the IMF slope is beyond the scope of this work.

Given galaxies in the early universe are likely dominated by low-metallicity stars, it is plausible for ξ_{ion} to systematically increase with redshift. Within the context of constant SFHs, sub-solar metallicity BPASS models show a higher ξ_{ion} at fixed metallicity compared to Starburst99 models. Constant SFH models with binaries from BPASSv2.2.1 show a strong dependence on stellar metallicity with the lowest stellar metallicity models showing the highest ξ_{ion} . At $t \sim 1$ Gyr, $Z \leq 1/5 Z_{\odot}$ models show $\log_{10}(\xi_{\text{ion}} [\text{Hz erg}^{-1}]) \sim 25.3\text{--}25.4$. Higher-metallicity BPASS models do not consider the effects of quasi-homogeneous evolution (Eldridge et al. 2017) and therefore show $\log_{10}(\xi_{\text{ion}} [\text{Hz erg}^{-1}]) \sim 25.2$.

Starburst99 models used in our analysis showed an opposite effect, where $Z = 0.002$ models show lower ξ_{ion} compared to $Z = 0.014$ models (note that in Starburst99 $Z_{\odot} = 0.014$ in contrast to $Z_{\odot} = 0.02$ in BPASS models). The highest ξ_{ion} achieved by Starburst99 Geneva rotational Z_{\odot} stellar tracks at $t = 1$ Gyr with a constant SFH is $\log_{10}(\xi_{\text{ion}} [\text{Hz erg}^{-1}]) \sim 25.2$. At higher metallicities, stars will lose angular momentum faster due to optically thick winds; therefore, lower-metallicity stars would have higher temperatures and longer main-sequence lifetimes (Leitherer et al. 2014). However, this increase in ionizing photons at lower metallicities is counteracted by the high abundance of W-R stars at Z_{\odot} . Therefore, the increase in ξ_{ion} with Z in Starburst99 models is modest (~ 0.07 dex increase between $1/7$ th Z_{\odot} to Z_{\odot} models). In BPASS models, effects of mass transfer between close binary stars results in the outer layers of massive red super-giants being removed efficiently, leading to a higher fraction of W-R stars and/or low-mass helium stars. Therefore, even at lower metallicities, there is an abundance of W-R stars in BPASS models.

5. Conclusions

In this work, we presented an analysis of the ionizing photon production efficiency (ξ_{ion}) of a mass/ K_s magnitude selected sample of star-forming galaxies at $z \sim 2$ observed by the ZFIRE survey using KECK/MOSFIRE. We analyzed how the ξ_{ion} correlates with observed/derived galaxy properties and combined our analysis of ξ_{ion} with $\text{H}\alpha$ EW and [340]–[550] colors, a commonly used diagnostic to analyze the stellar population properties of star-forming galaxies (e.g., Nanayakkara et al. 2017).

Our main conclusions are as follows:

1. The distribution of ξ_{ion} of our sample is similar to similar studies at $z \sim 2$, with a majority of galaxies falling below the canonical $\log_{10}(\xi_{\text{ion}} [\text{Hz erg}^{-1}]) = 25.2$ required to reionize the universe by $z = 6$.
2. By analyzing the ξ_{ion} correlation of our sample with galaxy properties such as UV continuum slope β , UV magnitude, stellar mass, $[\text{O III}]\lambda 5007/\text{H}\alpha$ ratio, and UV +IR and $\text{H}\alpha$ SFRs, we demonstrated that our results agree well with other studies of star-forming galaxies at $z \sim 2$.
3. We combined our analysis of ξ_{ion} with $\text{H}\alpha$ EW and rest-frame optical colors and analyzed the distribution of our sample with smooth SFH predictions from BPASSv2.2.1 stellar population models. We found that stellar models cannot self-consistently predict the observed distribution of galaxies in ξ_{ion} , $\text{H}\alpha$ EW, and [340]–[550] color space.

At fixed ξ_{ion} , the models always show lower $\text{H}\alpha$ EWs and redder [340]–[550] colors compared to the data.












4. We used Starburst99 stellar population models with various starburst properties to perform Monte Carlo simulations of galaxies in ξ_{ion} , $\text{H}\alpha$ EW, and [340]–[550] color space. Our random sampling of galaxies showed that statistically, it was unlikely to randomly select galaxies that populate our observed distribution.

Our analysis demonstrated that, within the context of the simple SFHs we explored, the stellar population models cannot self-consistently predict the observed distribution of $z \sim 2$ galaxies in ξ_{ion} , $\text{H}\alpha$ EW, and [340]–[550] color space. This may translate to a lack of hydrogen ionizing photons in UV bright galaxies in stellar population models. Thus, stellar population models may require additional changes to increase the ionizing photon output. In the future, we will extend the analysis presented here using Prospector (Leja et al. 2017) to investigate the individual SFHs of our sample at $z \sim 2$ and determine under which conditions the observed distribution of galaxies could be reproduced by nonparametric SFHs.

The authors recognize and acknowledge the very significant cultural role and reverence that the summit of Maunakea has always had within the indigenous Hawaiian community. We thank the anonymous referee for taking valuable time to provide thorough and constructive comments. We thank Irene Shivaie for providing the ξ_{ion} measurements used in the Shivaie et al. (2018) analysis. T.N., J.B., and R.B. acknowledge the Nederlandse Organisatie voor Wetenschappelijk Onderzoek (NWO) top grant TOP1.16.057. J.B. acknowledges support by Fundação para a Ciência e a Tecnologia (FCT) through national funds (UID/FIS/04434/2013) and Investigador FCT contract IF/01654/2014/CP1215/CT0003, and by FEDER through COMPETE2020 (POCI-01-0145-FEDER-007672). G.G.K. acknowledges the support of the Australian Research Council through the Discovery Project DP170103470. Parts of this research were supported by the Australian Research Council Centre of Excellence for All Sky Astrophysics in 3 Dimensions (ASTRO 3D), through project number CE170100013.

Facility: Keck:I (MOSFIRE).

ORCID iDs

Themiya Nanayakkara  <https://orcid.org/0000-0003-2804-0648>
 Jarle Brinchmann  <https://orcid.org/0000-0003-4359-8797>
 Karl Glazebrook  <https://orcid.org/0000-0002-3254-9044>
 Rychard Bouwens  <https://orcid.org/0000-0002-4989-2471>
 Lisa Kewley  <https://orcid.org/0000-0001-8152-3943>
 Kim-Vy Tran  <https://orcid.org/0000-0001-9208-2143>
 Michael Cowley  <https://orcid.org/0000-0002-4653-8637>
 Deanne Fisher  <https://orcid.org/0000-0003-0645-5260>
 Glenn G. Kacprzak  <https://orcid.org/0000-0003-1362-9302>
 Ivo Labbe  <https://orcid.org/0000-0002-2057-5376>
 Caroline Straatman  <https://orcid.org/0000-0001-5937-4590>

References

- Alcorn, L. Y., Tran, K.-V. H., Kacprzak, G. G., et al. 2016, *ApJL*, 825, L2
 Barkana, R., & Loeb, A. 2006, *MNRAS*, 371, 395
 Beckwith, S. V. W., Stiavelli, M., Koekemoer, A. M., et al. 2006, *AJ*, 132, 1729
 Bouwens, R. J., Aravena, M., Decarli, R., et al. 2016a, *ApJ*, 833, 72
 Bouwens, R. J., Illingworth, G. D., Franx, M., et al. 2009, *ApJ*, 705, 936

- Bouwens, R. J., Illingworth, G. D., Oesch, P. A., et al. 2015a, *ApJ*, **811**, 140
- Bouwens, R. J., Illingworth, G. D., Oesch, P. A., et al. 2015b, *ApJ*, **803**, 34
- Bouwens, R. J., Oesch, P. A., Illingworth, G. D., Ellis, R. S., & Stefanon, M. 2017, *ApJ*, **843**, 129
- Bouwens, R. J., Smit, R., Labbé, I., et al. 2016b, *ApJ*, **831**, 176
- Brammer, G. B., van Dokkum, P. G., & Coppi, P. 2008, *ApJ*, **686**, 1503
- Bruzual, G., & Charlot, S. 2003, *MNRAS*, **344**, 1000
- Calzetti, D., Armus, L., Bohlin, R. C., et al. 2000, *ApJ*, **533**, 682
- Calzetti, D., Kinney, A. L., & Storchi-Bergmann, T. 1994, *ApJ*, **429**, 582
- Cardelli, J. A., Clayton, G. C., & Mathis, J. S. 1989, *ApJ*, **345**, 245
- Chabrier, G. 2003, *PASP*, **115**, 763
- Chisholm, J., Rigby, J. R., Bayliss, M., et al. 2019, *ApJ*, **882**, 182
- Conroy, C. 2013, *ARA&A*, **51**, 393
- Cowley, M. J., Spitler, L. R., Tran, K.-V. H., et al. 2016, *MNRAS*, **457**, 629
- Draine, B. T. 2011, *Physics of the Interstellar and Intergalactic Medium* (Princeton, NJ: Princeton Univ. Press)
- Duncan, K., & Conselice, C. J. 2015, *MNRAS*, **451**, 2030
- Eldridge, J. J., Stanway, E. R., Xiao, L., et al. 2017, *PASA*, **34**, e058
- Erb, D. K., Pettini, M., Steidel, C. C., et al. 2016, *ApJ*, **830**, 52
- Finkelstein, S. L., Ryan, R. E., Jr., Papovich, C., et al. 2015, *ApJ*, **810**, 71
- Giacconi, R., Rosati, P., Tozzi, P., et al. 2001, *ApJ*, **551**, 624
- Glazebrook, K., Schreiber, C., Labbé, I., et al. 2017, *Natur*, **544**, 71
- Göberg, Y., de Mink, S. E., Groh, J. H., Leitherer, C., & Norman, C. 2019, *A&A*, **629**, A134
- Gunawardhana, M. L. P., Hopkins, A. M., Sharp, R. G., et al. 2011, *MNRAS*, **415**, 1647
- Haydon, D. T., Kruijssen, J. M. D., Hygate, A. P. S., et al. 2018, arXiv:1810.10897
- Hoversten, E. A., & Glazebrook, K. 2008, *ApJ*, **675**, 163
- Inami, H., Bacon, R., Brinchmann, J., et al. 2017, *A&A*, **608**, A2
- Kacprzak, G. G., Yuan, T., Nanayakkara, T., et al. 2015, *ApJL*, **802**, L26
- Kennicutt, R. C., Jr. 1983, *ApJ*, **272**, 54
- Kewley, L. J., Dopita, M. A., Leitherer, C., et al. 2013, *ApJ*, **774**, 100
- Kewley, L. J., Dopita, M. A., Sutherland, R. S., Heisler, C. A., & Trevena, J. 2001, *ApJ*, **556**, 121
- Kewley, L. J., Nicholls, D. C., & Sutherland, R. S. 2019, *ARA&A*, **57**, 511
- Kewley, L. J., Yuan, T., Nanayakkara, T., et al. 2016, *ApJ*, **819**, 100
- Kriek, M., & Conroy, C. 2013, *ApJL*, **775**, L16
- Kriek, M., Shapley, A. E., Reddy, N. A., et al. 2015, *ApJS*, **218**, 15
- Kuhlen, M., & Faucher-Giguère, C.-A. 2012, *MNRAS*, **423**, 862
- Labbé, I., Franx, M., Rudnick, G., et al. 2007, *ApJ*, **665**, 944
- Lam, D., Bouwens, R. J., Labbe, I., et al. 2019, *A&A*, **627**, A164
- Leitherer, C., Ekström, S., Meynet, G., et al. 2014, *ApJS*, **212**, 14
- Leja, J., Johnson, B. D., Conroy, C., van Dokkum, P. G., & Byler, N. 2017, *ApJ*, **837**, 170
- Mármol-Queraltó, E., McLure, R. J., Cullen, F., et al. 2016, *MNRAS*, **460**, 3587
- Matthee, J., Sobral, D., Best, P., et al. 2017a, *MNRAS*, **465**, 3637
- Matthee, J., Sobral, D., Boone, F., et al. 2017b, *ApJ*, **851**, 145
- McLean, I. S., Steidel, C. C., Epps, H. W., et al. 2012, *Proc. SPIE*, **8446**, 84460J
- Messias, H., Afonso, J., Salvato, M., Mobasher, B., & Hopkins, A. M. 2012, *ApJ*, **754**, 120
- Meurer, G. R., Heckman, T. M., & Calzetti, D. 1999, *ApJ*, **521**, 64
- Naidu, R. P., Tacchella, S., Mason, C. A., et al. 2019, arXiv:1907.13130
- Nakajima, K., Ellis, R. S., Iwata, I., et al. 2016, *ApJL*, **831**, L9
- Nakajima, K., Schaerer, D., Le Fevre, O., et al. 2018, *A&A*, **612**, A94
- Nanayakkara, T., Brinchmann, J., Boogaard, L., et al. 2019, *A&A*, **624**, A89
- Nanayakkara, T., Glazebrook, K., Kacprzak, G. G., et al. 2016, *ApJ*, **828**, 21
- Nanayakkara, T., Glazebrook, K., Kacprzak, G. G., et al. 2017, *MNRAS*, **468**, 3071
- Oke, J. B., & Gunn, J. E. 1983, *ApJ*, **266**, 713
- Persson, S. E., Murphy, D. C., Smee, S., et al. 2013, *PASP*, **125**, 654
- Reddy, N. A., Kriek, M., Shapley, A. E., et al. 2015, *ApJ*, **806**, 259
- Reddy, N. A., Oesch, P. A., Bouwens, R. J., et al. 2018, *ApJ*, **853**, 56
- Reddy, N. A., Steidel, C. C., Pettini, M., Bogosavljević, M., & Shapley, A. E. 2016, *ApJ*, **828**, 108
- Rees, G. A., Spitler, L. R., Norris, R. P., et al. 2016, *MNRAS*, **455**, 2731
- Robertson, B. E., Ellis, R. S., Furlanetto, S. R., & Dunlop, J. S. 2015, *ApJL*, **802**, L19
- Robertson, B. E., Furlanetto, S. R., Schneider, E., et al. 2013, *ApJ*, **768**, 71
- Salpeter, E. E. 1955, *ApJ*, **121**, 161
- Schaerer, D., Fragos, T., & Izotov, Y. I. 2019, *A&A*, **622**, L10
- Schreiber, C., Glazebrook, K., Nanayakkara, T., et al. 2018a, *A&A*, **618**, A85
- Schreiber, C., Labbé, I., Glazebrook, K., et al. 2018b, *A&A*, **611**, A22
- Scoville, N., Aussel, H., Brusa, M., et al. 2007, *ApJS*, **172**, 1
- Senchyna, P., Stark, D. P., Vidal-García, A., et al. 2017, *MNRAS*, **472**, 2608
- Shim, H., Chary, R.-R., Dickinson, M., et al. 2011, *ApJ*, **738**, 69
- Shin, M.-S., Trac, H., & Cen, R. 2008, *ApJ*, **681**, 756
- Shivaei, I., Reddy, N. A., Siana, B., et al. 2018, *ApJ*, **855**, 42
- Sparre, M., Hayward, C. C., Feldmann, R., et al. 2017, *MNRAS*, **466**, 88
- Spearman, C. 1904, *The American Journal of Psychology*, **15**, 72
- Spitler, L. R., Labbé, I., Glazebrook, K., et al. 2012, *ApJL*, **748**, L21
- Spitler, L. R., Straatman, C. M. S., Labbé, I., et al. 2014, *ApJL*, **787**, L36
- Stark, D. P., Ellis, R. S., Charlot, S., et al. 2017, *MNRAS*, **464**, 469
- Stark, D. P., Walth, G., Charlot, S., et al. 2015, *MNRAS*, **454**, 1393
- Steidel, C. C., Bogosavljevic, M., Shapley, A. E., et al. 2018, *ApJ*, **869**, 123
- Steidel, C. C., Rudie, G. C., Strom, A. L., et al. 2014, *ApJ*, **795**, 165
- Straatman, C. M. S., Labbé, I., Spitler, L. R., et al. 2014, *ApJL*, **783**, L14
- Straatman, C. M. S., Spitler, L. R., Quadri, R. F., et al. 2016, *ApJ*, **830**, 51
- Strom, A. L., Steidel, C. C., Rudie, G. C., et al. 2017, *ApJ*, **836**, 164
- Szokoly, G. P., Bergeron, J., Hasinger, G., et al. 2004, *ApJS*, **155**, 271
- Tang, M., Stark, D., Chevallard, J., & Charlot, S. 2019, *MNRAS*, **489**, 2572
- Tomczak, A. R., Quadri, R. F., Tran, K.-V. H., et al. 2016, *ApJ*, **817**, 118
- Tran, K.-V. H., Nanayakkara, T., Yuan, T., et al. 2015, *ApJ*, **811**, 28
- Urrutia, T., Wisotzki, L., Kerutt, J., et al. 2019, *A&A*, **624**, A141
- Wang, T., Schreiber, C., Elbaz, C., et al. 2019, *Natur*, **572**, 211
- Wilkins, S. M., Feng, Y., Di-Matteo, T., et al. 2016, *MNRAS*, **458**, L6
- Williams, R. J., Quadri, R. F., Franx, M., van Dokkum, P., & Labbé, I. 2009, *ApJ*, **691**, 1879
- Yuan, T., Nanayakkara, T., Kacprzak, G. G., et al. 2014, *ApJL*, **795**, L20